Geochemical variation in the Stimson formation of Gale crater: Provenance, mineral sorting, and a comparison with modern Martian dunes

C.C. Bedford, S.P. Schwenzer, J.C. Bridges, S. Banham, R.C. Wiens, O. Gasnault, E.B. Rampe, J. Frydenvang, P.J. Gasda

Icarus 341 (2020) 113622

Contents lists available at ScienceDirect

Icarus

journal homepage: www.elsevier.com/locate/icarus

Geochemical variation in the Stimson formation of Gale crater: Provenance, mineral sorting, and a comparison with modern Martian dunes

C.C. Bedford [a,b,*], S.P. Schwenzer [c], J.C. Bridges [d], S. Banham [e], R.C. Wiens [f], O. Gasnault [g], E. B. Rampe [b], J. Frydenvang [h], P.J. Gasda [f]

[a] Lunar and Planetary Institute, Universities Space Research Association, 3600 Bay Area Blvd., Houston, TX, USA
[b] Astromaterials and Exploration Science, NASA Johnson Space Center, Houston, TX, USA
[c] School of Environment, Earth and Ecosystem Sciences, The Open University, Walton Hall, Milton Keynes, MK7 6AA, UK
[d] Space Research Centre, School of Physics and Astronomy, University of Leicester, Leicester LE1 7RH, UK
[e] Imperial College London, London, UK
[f] Los Alamos National Laboratory, Los Alamos, NM, USA
[g] Institut de Recherche en Astrophysique et Planétologie, Université de Toulouse, CNRS, CNES, France
[h] Natural History Museum of Denmark, University of Copenhagen, Copenhagen, Denmark

A B S T R A C T

The Mars Science Laboratory *Curiosity* rover has encountered both ancient lithified and modern active aeolian dune deposits within Gale crater, providing an opportunity to study how aeolian processes have changed during Gale crater's geological history. This study uses data from the Chemistry and Camera (ChemCam) and Chemistry and Mineralogy (CheMin) instrument suites onboard *Curiosity* to; (1) constrain the diagenetic processes that lithified and altered the ancient aeolian Stimson formation, (2) investigate whether the geochemical signature in the Stimson formation is consistent with the aeolian mafic-felsic mineral sorting trend identified in the modern Bagnold dune fields in Gale crater, and (3) discuss the provenance of the Stimson sediments, comparing it to those identified in the modern dune and ancient river and lake deposits also analyzed along *Curiosity*'s traverse.

The ancient Stimson dune deposits that stratigraphically overlie the Gale fluvio-lacustrine units were analyzed in two locations; the Emerson and the Naukluft plateaus. ChemCam data show that the Stimson formation has subtle variations in MgO, Al_2O_3, Na_2O, and K_2O between the two localities. An agglomerative cluster analysis of the constrained Stimson dataset reveals five clusters, four of which relate to different proportions of mafic and felsic minerals analyzed by ChemCam. In general, the cluster analysis shows that the Emerson plateau has a greater proportion of mafic minerals and fewer coarse, felsic grains relative to the Naukluft plateau. This variation in mafic and felsic minerals between localities suggests a southwest to northeast net sediment transport direction due to aeolian mineral sorting dynamics preferentially transporting mafic minerals that are easier to saltate than the elongate, often coarser, felsic minerals. This derived transport direction for the Stimson formation supports that determined by sedimentological evidence and is opposite to that previously determined for the active Bagnold dunes inferring a change in the wind regime with time. An opposite sediment transport direction between the ancient and modern dunes in Gale crater further supports geochemical and mineralogical evidence that suggests different basaltic source regions. Compositionally, the bulk Stimson formation is most similar to the subalkaline basalt source region that is inferred to be the dominant sediment source of the fluvio-lacustrine Bradbury group. This is likely the result of the Stimson formation and basaltic Bradbury group sediments sharing a similar local basaltic source region such as the rim and walls of Gale crater.

1. Introduction

Gale crater was chosen as the site for the NASA Mars Science Laboratory (MSL) *Curiosity* rover due to Aeolis Mons: the ~5 km tall, layered, central mound informally named Mt. Sharp. Orbital remote sensing instruments have detected secondary minerals in the lower units and anhydrous mineral assemblages within large-scale cross-bedding in the upper units (Deit et al., 2013; Fraeman et al., 2013; Grotzinger et al., 2012; Milliken et al., 2010; Thomson et al., 2011; Wray, 2013). This unconformity has been identified in several layered mound deposits situated in craters at other locations on Mars (Ehlmann and Buz, 2015; Malin et al., 2000; Thomson et al., 2011) and may be a result of the change from warm and wet conditions to the cold and dry global environment seen today (Fraeman et al., 2016; Grotzinger et al., 2012; Milliken et al., 2010; Thomson et al., 2011; Wray, 2013). Our study investigates the geochemistry of a preserved aeolian unit called the

* Correspondence to: C. C. Bedford, Lunar and Planetary Institute, Universities Space Research Association, 3600 Bay Area Blvd., Houston, TX, USA.
E-mail addresses: candice.c.bedford@nasa.gov (C.C. Bedford), susanne.schwenzer@open.ac.uk (S.P. Schwenzer), j.bridges@leicester.ac.uk (J.C. Bridges), s.banham@imperial.ac.uk (S. Banham), rwiens@lanl.gov (R.C. Wiens), olivier.gasnault@irap.omp.eu (O. Gasnault), elizabeth.b.rampe@nasa.gov (E.B. Rampe), jfrydenvang@snm.ku.dk (J. Frydenvang), gasda@lanl.gov (P.J. Gasda).

https://doi.org/10.1016/j.icarus.2020.113622
Received 1 November 2019; Received in revised form 18 December 2019; Accepted 4 January 2020
Available online 15 January 2020

Stimson formation (Figs. 1A, B & 2) that was deposited after a prolonged period of aeolian deflation, which likely represents the end of a relatively warm and wet period in Gale crater (Banham et al., 2018; Fraeman et al., 2016). By investigating the geochemistry of this unit and comparing it to the other ancient and modern sedimentary deposits in Gale crater, we aim to constrain sedimentary processes and provenance throughout Gale's geological history, particularly those that relate to aeolian processes which have dominated the Martian surface for several billion years (Carr, 2007; Craddock, 2012).

Studies of aeolian dunes derived from basaltic source rocks on the Earth have demonstrated that major element chemistry can give information on mineral sorting processes, which in turn approximates the net resultant wind direction at the time of deposition (Baratoux et al., 2011; Mangold et al., 2011; Mountney and Russell, 2004; Rubin and Hunter, 1987; Swanson et al., 2016). Dunes derived from basaltic sediments typically demonstrate enhanced transport of mafic minerals (olivine and pyroxene) over felsic minerals (feldspar) as their generally finer grain size and rounder shape make them easier to saltate in comparison to the elongate feldspar grains (e.g., Baratoux et al., 2011; Mangold et al., 2011). Therefore, the further a basaltic dune deposit is from its source, the more enriched in mafic grains it will become relative to felsic grains (Baratoux et al., 2011; Mangold et al., 2011). A mafic-felsic mineral sorting regime has also been identified in wind-blown soil deposits and basaltic dunes on Mars using orbital and rover data (Cousin et al., 2015; Lapotre et al., 2017; Meslin et al., 2013; O'Connell-Cooper et al., 2018; Rampe et al., 2018; Stockstill-Cahill et al., 2008). Similar to the terrestrial wind-blown deposits, the soil deposits of Gale crater contain a greater abundance of felsic minerals in the coarse size fraction (Cousin et al., 2015; Meslin et al., 2013). The active Bagnold dunes in Gale crater (Fig. 1B) also contain felsic minerals as the coarsest grains (Cousin et al., 2017), but show an overall greater abundance of olivine compared to feldspar in the coarser grain size fraction (>250 μm), and a lower abundance of volatiles compared to the inactive, dust-covered soils analyzed along the traverse (Cousin et al., 2017, 2015; O'Connell-

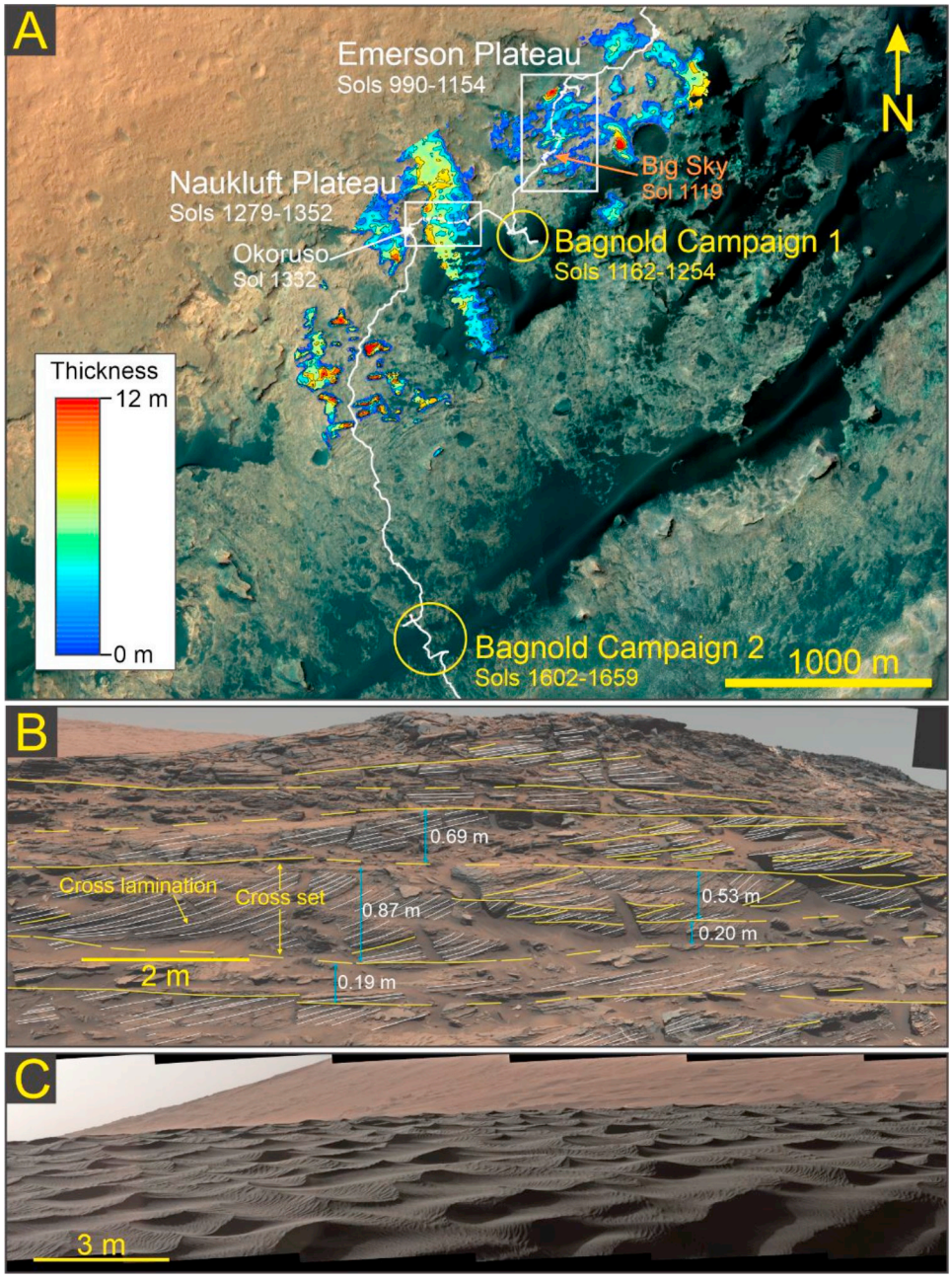

Fig. 1. Context images for the Stimson formation sandstone. A) An isopach map of the Stimson formation, white line shows the rover traverse and triangles indicate waypoints. The locations of drilled, unaltered Stimson samples and the Bagnold dune campaigns are also shown. To calculate the preserved thickness (isopach), the unconformity was mapped where it intersected the ground-surface using satellite images and Digital Elevation Models (Watkins et al., 2016). An interpolated surface was generated based on the vertical position of the unconformity (nearest neighbour) to create a depth map. This depth map was subtracted from the present-day land surface, to give a thickness map of the remnant Stimson. Where the thickness of Stimson was 0 or less is where the Stimson has been totally removed by erosion, and these areas were deleted. B) Annotated Mast camera (Mastcam) image of the lithified Stimson formation at Williams Peak in the Emerson Plateau (mcam04777, sol 1099). Annotations show the cross laminations and cross set thicknesses present within the lithified deposit (Banham et al., 2018), and C) Mastcam mosaic of the modern Bagnold dune deposits (mcam05410, sol 1192).

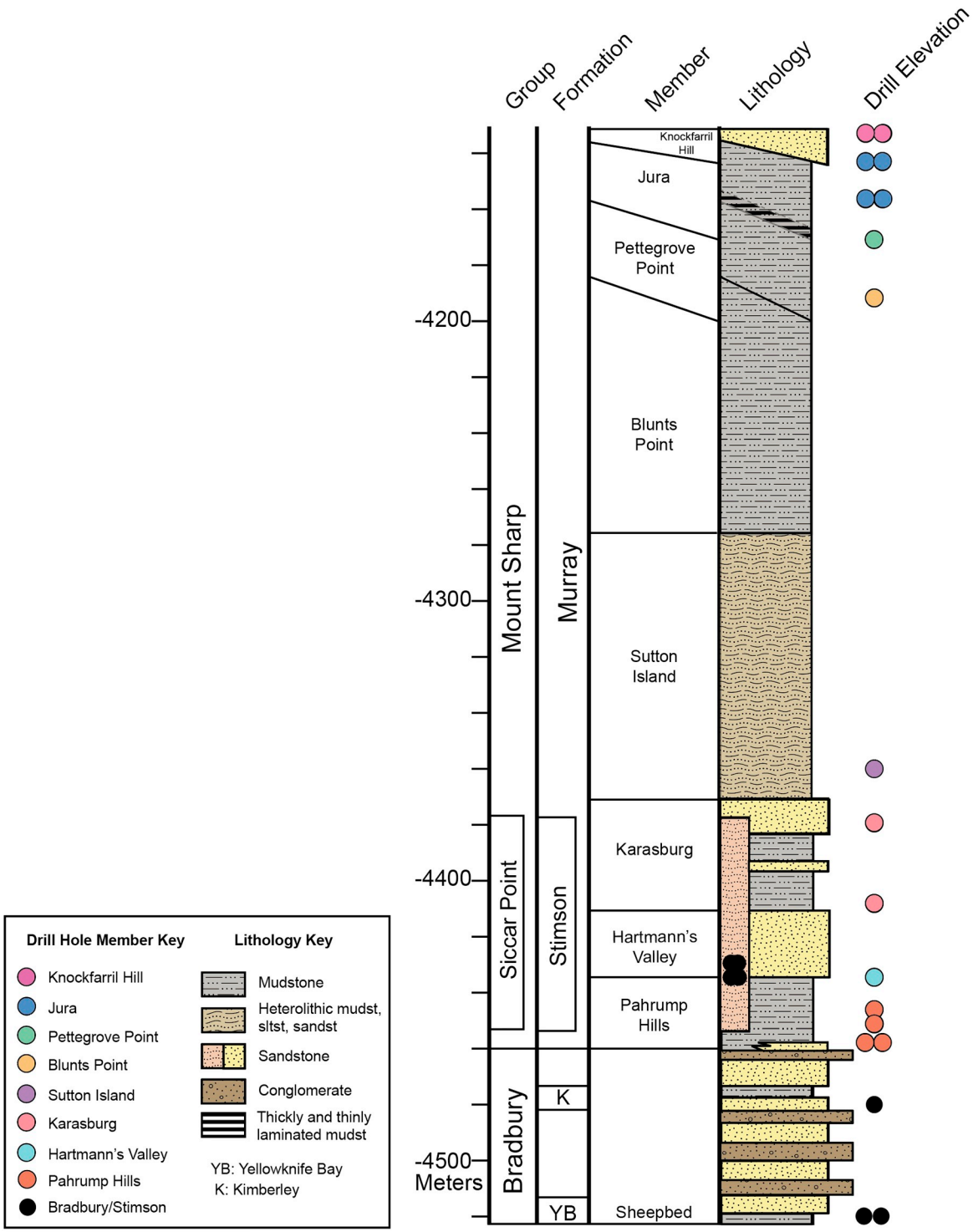

Fig. 2. A stratigraphic log from Edgar et al., 2020 showing an overview of the Sedimentology and Stratigraphy observed by the Mars Science Laboratory Curiosity Rover according to elevation (m). This stratigraphic log illustrates the stratigraphic relationships of the Gale crater geological units traversed by the Curiosity rover from the Bradbury landing site to the Vera Rubin Ridge.

Cooper et al., 2018; Pan and Rogers, 2017; Rampe et al., 2018). This difference in olivine abundance between the modern Martian dunes and soils has several possible explanations; a result of the coarser fraction experiencing less alteration than the Aeolis Palus soils (Cousin et al., 2017; O'Connell-Cooper et al., 2018), a greater maturity of mineral sorting for the dunes (Cousin et al., 2017; Lapotre et al., 2017), or a greater abundance of olivine-rich sediment source rocks (O'Connell-Cooper et al., 2018), all of which still correlate to the aeolian mafic-felsic mineral sorting regime described previously and identified on the Earth.

One aim of this study is to determine the mineral sorting regime of the ancient Stimson sediments using a cluster analysis of the Laser-Induced Breakdown Spectroscopy (LIBS) measurements of the Chemistry and Camera (ChemCam) instrument suite; and to compare these results to the mineral sorting dynamics of the modern Bagnold dunes. An advantage to the small sampling size (<1 mm diameter) of the ChemCam LIBS laser is that it is more likely to target individual minerals in

coarser grained targets (Cousin et al., 2017; Rivera-Hernández et al., 2019). This is in contrast to the Alpha Particle X-Ray Spectrometer (APXS) geochemical instrument on-board *Curiosity* whose analyses are more representative of bulk geochemistry due to the larger size (17 mm diameter) of the sampling area (Gellert and Clark, 2015; Siebach et al., 2017a). Previous studies have shown that geochemical variations in the ChemCam dataset for Gale crater's lithified and unlithified sediment deposits are associated with mafic and felsic minerals (Bedford et al., 2019; Cousin et al., 2017; Deit et al., 2016; Mangold et al., 2016; Meslin et al., 2013) which makes it a promising dataset for identifying mineral sorting in the ancient Stimson formation. We use a multivariate cluster analysis to group over 330 ChemCam LIBS geochemical data points according to their relative compositional similarity, which, in the case of the LIBS data, will isolate groups that likely reflect the different proportions of minerals in the sediments provided analyses of alteration features (i.e., mineral veins) have been removed (Cousin et al., 2015; Gasnault et al., 2013; Meslin et al., 2013). Comparing the proportion of different clusters between the two Stimson localities – the Emerson plateau and Naukluft plateau (Fig. 1A) – should therefore constrain the effect of mineral sorting between these two sites in the Stimson dune field.

Basaltic dune studies also show that bulk geochemical variation can be a result of changes in dominant sediment provenance with time on Earth and Mars (Achilles et al., 2017; Baratoux et al., 2011; Lapotre et al., 2017; Mangold et al., 2011; Mountney and Russell, 2004; O'Connell-Cooper et al., 2018; Pan and Rogers, 2017; Rampe et al., 2018). We therefore also use a density contour analysis of ChemCam LIBS data to compare the Stimson formation bulk geochemistry to that of the modern dunes and ancient fluvio-lacustrine deposits in Gale crater in order to identify changes in dominant source regions throughout geological time.

1.1. Geological context of the Stimson formation

The stratigraphy of Gale crater is composed of sedimentary rocks deposited in an ancient river-lake system that likely existed between 3.8 and 3.1 Ga ago (Deit et al., 2013; Grotzinger et al., 2015, 2014; Stack et al., 2019), with minor aeolian units, or units of unknown affinity, unconformably draping the older lake deposits (Banham et al., 2018; Bryk et al., 2019). Stratigraphy within Gale crater is divided into three distinct groups based on their lateral extent, separation by major discontinuities, and depositional origins into the Bradbury, Mt. Sharp, and Siccar Point groups (Fig. 2).

The Bradbury group is characterized predominantly by fluvial, fluvio-deltaic, and lacustrine deposits (Grotzinger et al., 2015, 2014; Stack et al., 2019; Vasavada et al., 2014; Williams et al., 2013). Bradbury is the lowest stratigraphic group analyzed by *Curiosity* and contains sediments likely derived from a tholeiite-dominated source (Bedford et al., 2019; Edwards et al., 2017), but with certain parts of the succession (i.e., the Kimberley formation) also containing sediments sourced from more alkaline provenances (Bedford et al., 2019; Deit et al., 2016; Siebach et al., 2017a; Treiman et al., 2016). It is likely that the main tholeiite source region of the Bradbury group sediments was also plagioclase-phyric, which resulted in the coarser plagioclase minerals being segregated from the finer mafic component during transportation in the ancient fluvio-lacustrine system (Siebach et al., 2017a). *Curiosity*'s investigation of the Bradbury group began once it landed in Gale crater in 2012 and ended on sol 753 of the mission when it entered the Pahrump Hills locality that marked the first strata encountered by *Curiosity* within the Mt. Sharp group (Grotzinger et al., 2015).

The Mt. Sharp group is dominated by finely-laminated mudstone deposited in shallow and deep lake waters (Fedo et al., 2018; Hurowitz et al., 2017), where sediments were transported to the lake margin by fluvial processes, before being redistributed within the deeper sections of the lake by plunging hyperpycnal flows (Stack et al., 2019). The Bradbury and Mt. Sharp groups are hypothesized to have accumulated coevally within the same wider fluvio-lacustrine system, as the groups are interpreted to interfinger at their contact (Grotzinger et al., 2015). The majority of the Mt. Sharp group traversed by *Curiosity* is stratigraphically younger than the Bradbury group as these outcrops are observed at higher elevations, and the strata across the north of Aeolis Mons are near-horizontal (Grotzinger et al., 2015). Although the Mt. Sharp group is also largely basaltic in geochemistry, the bulk composition of the Mt. Sharp group mudstone is distinct from that of the Bradbury group mudstone, having a more silica-rich basalt as the dominant source (Bedford et al., 2019). Additionally, the detection of tridymite in the highly (>60 wt%) silica-rich locality of Marias Pass suggests that the sediment in this area could have been derived from an evolved, silicic igneous source (Czarnecki et al., 2018; Morris et al., 2016).

The Mt. Sharp group is unconformably overlain by the Siccar Point group (Fig. 2), which is a draping unit deposited on a deflation surface (Banham et al., 2018; Fraeman et al., 2016; Kite et al., 2013; Watkins et al., 2016). At present, the Stimson formation is the only unit within the Siccar Point group encountered so far by the rover, however the Greenheugh pediment is observed to overlay the Murray formation at higher elevations of the flank of Aeolis Mons, and is interpreted to lay on the same unconformity dividing the Siccar Point and Mt. Sharp groups (Bryk et al., 2019). The unconformity on which the Stimson formation accumulated represents an undulating palaeo surface. Watkins et al. (2016) mapped this unconformity and demonstrated that the surface rises ~140 m in elevation towards the south over a distance of 2 km.

Curiosity investigated the sedimentology, chemistry and mineralogy of the Stimson formation between Sols 987–1455 (Fig. 1), which was interpreted to represent the preserved remnants of an ancient aeolian dune field (Banham et al., 2018). Sand grains observed using the MAHLI instrument have a high roundness and sphericity, and bimodal grain size distribution (major modal peak of 250 μm and minor modal peak ~850 μm), which indicates that the grains were transported by saltation and surface creep by the wind (Bagnold, 1937; Kok et al., 2012; Sharp, 1963). Cross sets, measured up to 1 m in thickness across the Emerson plateau (Fig. 1.B) represent the migration of aeolian dunes up to 15 m high (Banham et al., 2018). The lack of phyllosilicates (Yen et al., 2017) fine-grained interdune deposits or fluvial facies deposits (i.e., laminated mudstones or conglomerate beds), indicate that the system accumulated by dry aeolian processes, in an arid environment (Banham et al., 2018).

The inclined unconformity formed by deflation and the slope-draping nature of the dry-aeolian system suggests the Stimson formation accumulated after a protracted period of aridity. A substantial period of time would have passed for the climate to shift from humid conditions which supported the fluvio-lacustrine system that deposited the Bradbury and Mt. Sharp groups, to the arid environment which supported deposition of the Stimson formation (Watkins et al., 2016; Banham et al., 2018). As such, the Stimson formation is one of the youngest, in situ, lithified units investigated by *Curiosity* to date (Banham et al., 2018).

The presence of Mg-rich ridges (Léveillé et al., 2014), calcium-sulfate mineral veins (Nachon et al., 2014; Rapin et al., 2016) and fracture-associated alteration halos (Frydenvang et al., 2017; Yen et al., 2017) show a long history of groundwater activity in Gale crater (Bridges et al., 2015; McLennan et al., 2014). The lithification of the Stimson formation and the presence of post-depositional aqueous alteration features such as calcium-sulfate veins and cement, fracture associated halos and concretions within the Stimson formation (Fig. 3) suggests that even after the surface became arid, sufficient groundwater was present within the subsurface post-deposition to allow diagenesis to take place (Banham et al., 2018; Chan et al., 2012; Frydenvang et al., 2017; Potter-McIntyre et al., 2014; Potter et al., 2011; Yen et al., 2017). Based on the comparable geochemistry to the surrounding bedrock, concretions found in Stimson rocks are hypothesized to have formed in closed-system conditions (Banham et al., 2018; Siebach et al., 2017a), meanwhile, the veins and halos have a unique chemistry indicative of open-system aqueous alteration (Hausrath et al., 2018; Yen et al., 2017).

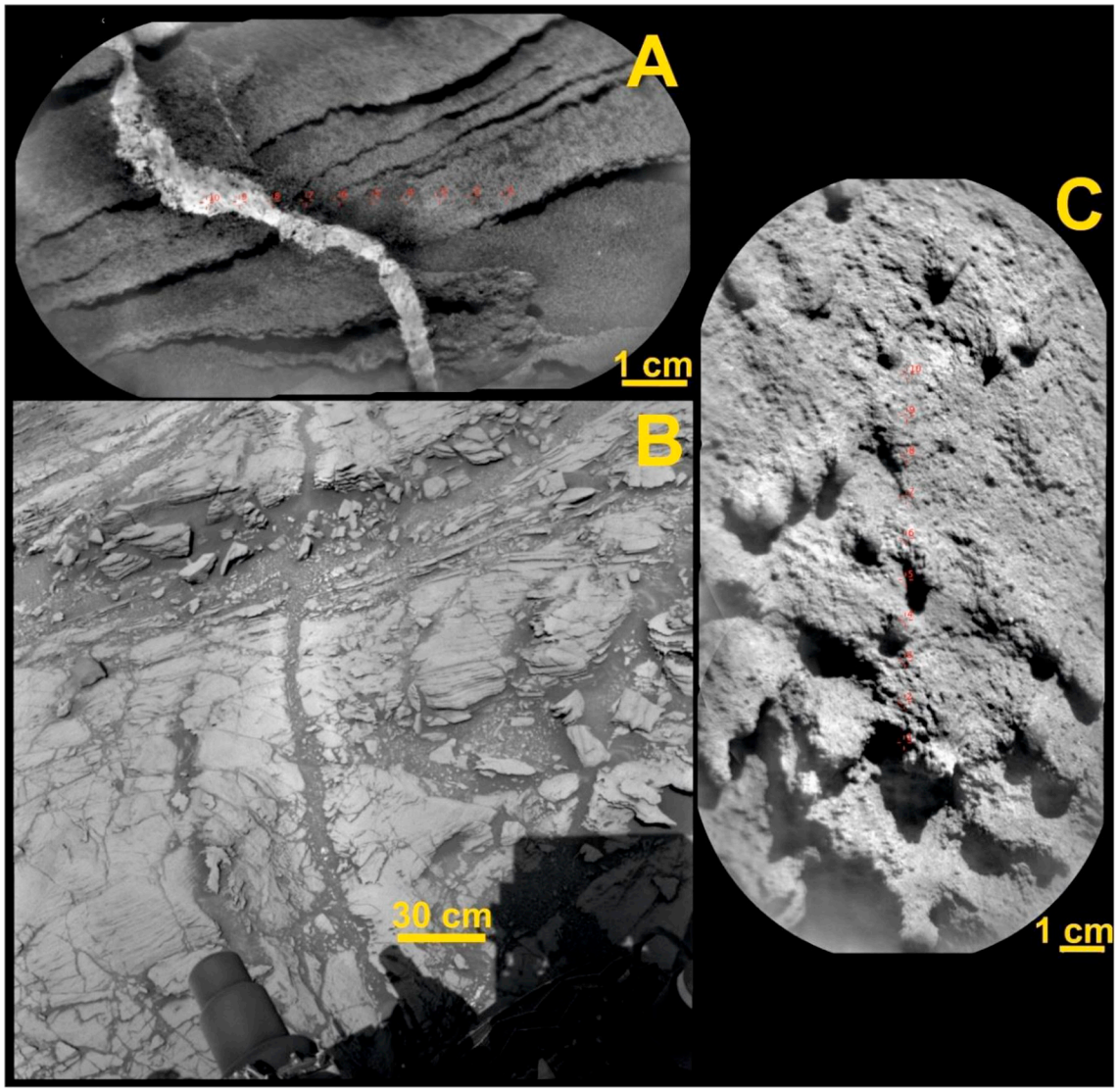

Fig. 3. ChemCam Remote Micro-Imager (RMI) and Navcam images of alteration features in the Stimson sandstone. A) shows an RMI mosaic of the O'Brien's Creek ChemCam target (sol 1090) that sampled a calcium-sulfate vein, B) is a Navcam image (ncam00354, sol 1094) of an alteration halo and C) is the RMI mosaic of ChemCam target Katwitwi (sol 1305) showing concretions that are common within Stimson, especially at the Naukluft Plateau.

1.2. Description of Stimson localities

The Stimson formation has a total outcrop coverage of 20 km^2 (Kronyak et al., 2019), which outcrops in 3 main geographically distinct areas on the traverse: Emerson plateau, Naukluft plateau, and Murray Buttes. The ChemCam instrument was used to analyze the Stimson in two of these areas (Fig. 1A): the Emerson plateau (sols 990–1154) which covers the Marias Pass and Bridger Basin localities, and the Naukluft plateau (sols 1279–1352). Analysis at the Murray Buttes area was not possible as the outcrop was inaccessible and was situated beyond the useful range of the LIBS instrument. As a result, this study focuses solely on geochemical and mineralogical data collected at the Emerson and Naukluft plateaus.

1.2.1. The Emerson Plateau

The Stimson formation at the Emerson plateau area is characterized by outcrops of blocky, dark grey sandstones up to ~7 m tall which unconformably overlies the smooth, tan-colored outcrop of the Mt. Sharp group (for a detailed description of this locality, see Banham et al., 2018). Here, the Stimson formation is composed predominantly of simple cross sets, which are typically between 0.3 and 1.0 m thick (Fig. 1B). The cross sets are formed of cross laminations that are uniform in thickness along their length from the upper to lower bounding surface and have an average measured thickness of 4 mm (Banham et al., 2018). Where outcrop permits, bounding surfaces can be traced for a distance of ~30 m, are largely sub-horizontal and can undulate by a few decimeters along their length. These bounding surfaces, which define the upper and lower surfaces of the cross sets are interpreted to be interdune surfaces formed by the scour pit that preceded the dune as it advanced (Banham et al., 2018; Kocurek, 1991). At a few locations, such as Marias Pass, concretions measured to between 20 and 40 mm in diameter can be observed overprinting the sedimentary texture, however, these concretions are not ubiquitous (Banham et al., 2018).

1.2.2. The Naukluft Plateau

The Stimson formation at Naukluft is exposed on a plateau ¼ km wide, measured east to west (Fig. 1A). The total thickness of the Stimson formation here ranges between ~0.5–10 m, based on the interpolation of the base of the unconformity (Watkins et al., 2016; Fig. 1A). In this area, the Stimson is characterized by an outcrop composed of trough-cross bedded sandstones, similar to those exposed in the Emerson area. Measurement of set thickness here is difficult due to the lack of

vertical exposure across the plateau. In this area, there is a prevalence of concretions (Fig. 3C) with diameters of up to a few 10 s mm. The occurrence of these concretions can range from sporadically distributed within a single cross set, through to completely overprinting the sedimentary facies, all but masking evidence of crossbedding. Both from the surface and orbital images, polygonal fractures with widths on average 7.5 m (Kronyak et al., 2019), similar to the fracture-halos observed in the Emerson plateau can be identified. At both localities these halos (Fig. 3.B) showed clear chemical and mineral alteration with high SiO_2 > 80 wt% (Frydenvang et al., 2017), low crystalline mineral abundances < 35 wt%, and a notable amorphous component > 65 wt% (Morrison et al., 2018b; Yen et al., 2017).

1.3. The Bagnold dunes as a modern analogue

Gale crater contains several modern active aeolian dune fields, which occupy the crater moat surrounding Mt. Sharp (Hobbs et al., 2010). The Bagnold dune field (Fig. 1A & C), the only dune field to fall within the MSL landing ellipse, has been the subject of two science campaigns during the traverse (Bridges and Ehlmann, 2018; Lapotre and Rampe, 2018). The first campaign analyzed two barchan dunes, informally named Namib dune and High dune between sols 1162–1254 (Bridges and Ehlmann, 2018). During this campaign, CheMin analyzed a scooped sample named "Gobabeb" on the stoss slope of Namib dune (Achilles et al., 2017). The second campaign analyzed linear dunes at the Nathan Bridges dune and Mount Desert Island ripple field between sols 1602–1659 (Lapotre and Rampe, 2018) with the scooped sample named "Ogunquit Beach" taken from a ripple trough at Mount Desert Island (Rampe et al., 2018). CheMin analyses indicate these dunes largely contain basaltic minerals such as olivine, plagioclase feldspar and pyroxene (Achilles et al., 2017; Rampe et al., 2018) and show evidence that they have scavenged local material from underlying bedrock such as anhydrite, hematite or a silica-rich amorphous component (Achilles et al., 2017; Rampe et al., 2018). A ChemCam study in the first dune campaign and Dynamic Albedo of Neutron (DAN) instrument measurements for both dune campaigns also show that the dunes are dehydrated relative to the surrounding bedrock and soils, suggesting that the more hydrated, fine-grained portion (<100 μm) of the Aeolis Palus soils are absent from these active deposits (Cousin et al., 2017; Gabriel et al., 2018). The Bagnold dune field will be used in this study as a modern-day analog to the Stimson formation, providing insights into ancient aeolian processes such as the mineral sorting, changes in wind direction and changes in sediment source region discussed previously.

2. Methods for data acquisition and processing

2.1. The chemistry and Camera (ChemCam) instrument suite

We primarily use geochemical data from the ChemCam instrument suite (Maurice et al., 2012; Wiens et al., 2012). ChemCam uses LIBS to generate spectral analyses of a target rock or soil at standoff distances (Maurice et al., 2012; Wiens et al., 2012). Most of the targets are chosen below 5 m from the rover mast (Maurice et al., 2016), but signal was obtained up to 8.5 m on some targets (Meslin et al., 2019). ChemCam also has a Remote Micro-Imager (RMI) that takes high-resolution images of targets before and after the LIBS spectral data are acquired to provide geological context (Le Mouélic et al., 2015; Maurice et al., 2012). LIBS spectral analyses are converted into major, minor and trace element abundances after data have been pre-processed to remove effects such as ambient light background and noise (Wiens et al., 2013). Then, a quantitative analysis is attained using a combination of partial least squares sub-models and independent component analysis (Anderson et al., 2017; Clegg et al., 2017; Forni et al., 2013). Observation point analyses are averages of 30–50 spectra, where each laser pulse produces a spectrum. The first five spectra are left out to minimize surface dust contamination (Clegg et al., 2017; Wiens et al., 2013). ChemCam makes observations in a raster pattern on each target (Maurice et al., 2016). However, individual observation points rather than averages of entire raster patterns are used here to evaluate data that is more representative of the different mineral grains and sandstone cement present in the rock. ChemCam uncertainty has been presented as accuracy and precision (Wiens et al., 2012) and shown in Supplementary information (Table A.1). Accuracy is determined by the root mean square error product of prediction (RMSEP) for representative geological samples that share abundance ranges similar to those in the calibration regression models (Clegg et al., 2017). ChemCam instrument precision is the equivalent of the 'error' (precision) presented with APXS results, and is calculated as the variation observed across the 25 shots that make up the average spectrum for each observation point (Blaney et al., 2014), or across targets from a uniform unit (Mangold et al., 2016).

2.2. ChemCam target classification and methods to minimize the geochemical effects of alteration in the bulk rock dataset

ChemCam observation points have been grouped into bulk rock, secondary diagenetic features, unconsolidated sediments, and float datasets based on targets imaged by RMI and the other scientific cameras on-board *Curiosity*: Mast camera (Mastcam) and the Mars Hand Lens Imager (MAHLI) (Edgett et al., 2012; Malin et al., 2017). Mastcam comprises two, fixed-focal length, multispectral, colour CCD imagers (Malin et al., 2017). These cameras are situated on *Curiosity*'s mast 24.2 cm apart and are positioned ~2 m from the surface (Malin et al., 2017). The left Mastcam (M-34) has a focal length of 34 mm, with a field of view (FOV) of 20° x 15°, and a pixel scale of 0.22 mrad/pixel, while the right Mastcam (M-100) has a 100 mm focal length, a FOV of 6.8° × 5.1°, and a 0.074 mrad/pixel scale of sampling (Malin et al., 2017). Data from this instrument suite were used to analyze geological targets at the scale of the outcrop. Images taken by MAHLI of ChemCam targets are used in this study to support those from the ChemCam RMI. MAHLI is situated on the turret at the end of the *Curiosity* rover's arm, and uses a 2-megapixel colour CCD camera to analyze the textures, structures and morphologies present at *Curiosity*'s field site at the finest grain size possible 0.0042 mm (silt) for *Curiosity*'s cameras (Edgett et al., 2012; Mangold et al., 2017).

Classification has been done on individual ChemCam observation points as many targets sample both unaltered rock, soil and alteration features. Bulk rock analyses are defined here as those that have targeted an indurated, lithified unit, commonly containing sedimentary structures (e.g., bedding or laminations) and secondary structural features (e.g., bedrock fractures). It is important to note that bulk rock analyses are not truly alteration-free as the Stimson formation has undergone compaction and cementation during diagenesis. Provided that the diagenesis that formed the cement was isochemical and formed in a closed system, the chemistry of the Stimson formation bulk rock dataset should be largely representative of the aeolian sand deposits before they became lithified. The Stimson formation contains abundant concretionary features in the bedrock which are likely a result of preferential cementation of the Stimson sands (Banham et al., 2018; Chan et al., 2012; Potter-McIntyre et al., 2014; Potter et al., 2011). ChemCam and APXS analyses of concretionary Stimson show that they have the same geochemical compositions to non-concretionary Stimson (Appendix B; Banham et al., 2018; Siebach et al., 2017b) and are hypothesized to relate to closed-system diagenesis that preserves bulk rock geochemistry (Banham et al., 2018; Siebach et al., 2017b). Therefore, concretionary features are included in the bulk rock dataset as their geochemical composition is likely representative of the dune sand deposit prior to lithification. In order to isolate the effects of non-isochemical alteration in the ChemCam database, observation points that have analyzed any obvious, open-system diagenetic feature such as calcium-sulfate mineral veins and fracture-associated halos (e.g., Fig. 2A & B) have been removed and placed into an alteration dataset. As this study focuses on bulk rock geochemistry of the Stimson formation, any observation

points on float have also been removed from the main bulk rock dataset as their stratigraphic position cannot be fully determined.

Sediments affected by extensive alteration largely become enriched in volatile elements (S, Cl, H) that are not normally quantified in the standard ChemCam dataset. Hence, any observation point that has targeted open-system alteration features usually shows a depletion in the non-normalized total sum of oxides. For this reason, observation points with total sum of oxides outside of the range 95–105 wt% are removed from the dataset to make the constrained bulk rock dataset used to estimate the bulk rock compositions. This method has the added benefit of removing targets that have been contaminated by Martian surface dust and soil due to their higher concentrations of volatiles (Bish et al., 2013; Ehlmann et al., 2017; Lasue et al., 2018; Meslin et al., 2013; O'Connell-Cooper et al., 2017). Though the active aeolian dunes generally have less volatiles compared to inactive Gale crater soils (Cousin et al., 2017; Gabriel et al., 2018), volatile contents are still high enough to complicate a direct comparison of the active dunes and constrained Stimson dataset. In particular, S commonly pairs with Ca and Mg to form calcium- and magnesium-sulfates (Nachon et al., 2014; Rapin et al., 2016; Schieber et al., 2017; Schwenzer et al., 2016), although Bagnold dune analyses do not show significant enrichments in CaO and MgO relative to bulk Stimson suggesting that the influence of sulfates is low (O'Connell-Cooper et al., 2017). Hence, we have only removed Bagnold dune analyses outside a total range of 80–105 wt%. Then, we normalized the data to 100% to make the constrained Stimson and Bagnold dune datasets comparable to one another. A possible residual distance effect on the ChemCam geochemical composition of targets is under investigation on targets analyzed at distances >4 m from the rover, therefore we also excluded 8 targets that were taken beyond this distance to avoid its effect on the results. The constrained bulk rock dataset used in this study is provided in the Supplementary materials, Appendix C.

2.3. Statistical approach

In total, 331 observation points constitute the constrained Stimson bulk rock dataset; 150 within the Emerson plateau and 181 for the Naukluft plateau (See Table C.1 in the Supplementary material for the observation points used in the study). The ChemCam LIBS laser has a relatively small footprint (350–750 μm for distances of 3–7 m from the rover mast; Maurice et al., 2012), so target analyses are often not representative of whole rock compositions, particularly if the target is coarse-grained (grain diameter > 1 mm) as individual mineral grains are more likely to be analyzed (Cousin et al., 2017). Due to the large number of observation points acquired by ChemCam, a statistical approach is implemented to identify the geochemical trends and bulk compositions for the stratigraphic units. The statistical methods applied here include a simple univariate description of the data in the form of basic statistics (i.e., mean, mode, range), followed by the estimation of bulk composition with multivariate density contour plots. Density contour plots display the data population across two variables as isolines (contours) representative of the density of smoothed data within each pixel defined by the bin size (Bedford et al., 2019; Eilers and Goeman, 2004). Data densities are smoothed according to Eilers and Goeman (2004) and contours are generated using MATLAB (2003). This method has proven useful to illustrate the compositional foci and geochemical trends across each of the fluvio-lacustrine stratigraphic groups and igneous rocks within Gale crater (Bedford et al., 2019; Edwards et al., 2017). A density contour analysis also has the additional benefit of effectively simulating bulk rock compositions of the Emerson plateau and Naukluft plateau localities.

Following the density contour analysis, subgroups relating to mineral proportions within the Stimson formation are calculated using an agglomerative cluster algorithm with Minitab 17 Statistical Software (2010). This algorithm defines each data point as a cluster, then combines the two closest clusters into a new one at each step (Schuenemeyer and Drew, 2011). The similarity or correlation of each Cluster is presented in the dendrogram as a similarity level, where higher similarity levels represent stronger correlations between Clusters (Schuenemeyer and Drew, 2011). The similarity level is also used to identify the number of Clusters in the dataset. In this study, if there is an abrupt change in similarity or distance values between steps (i.e., the difference in similarity is >5.00 where previously it was <1.00), a new Cluster is identified. Cluster analysis is a useful method of distinguishing previously undefined groups that exist within a multivariate dataset (Schuenemeyer and Drew, 2011). For the constrained Stimson dataset, we use the complete linkages measure of association for Euclidean distances with all major element oxides as variables as this method provided the best fit to the dataset. Hierarchical clustering methods were successfully used in previous cluster analysis studies of Gale crater sediments (Gasnault et al., 2019, 2013). The Euclidean distance calculates the square-root of the sum of the squared differences between the observations for each variable within a cluster (Schuenemeyer and Drew, 2011). For each step, the complete linkage method merges together clusters with the smallest maximum pairwise distance, hence, each cluster remaining will be the most dissimilar from each other (Schuenemeyer and Drew, 2011). Variables (SiO_2, TiO_2, Al_2O_3, FeO_T, MgO, CaO, Na_2O, K_2O) were standardized in order to minimize the effect of scale differences.

2.4. The chemistry and mineralogy (CheMin) instrument suite

The CheMin instrument on-board the *Curiosity* rover is housed within the body unit and generates X-ray diffraction (XRD) patterns of drilled or scooped samples (Blake et al., 2012; Morrison et al., 2018b). These diffraction patterns are used alongside data from the Sample Analysis at Mars (SAM) and APXS instruments to identify the mineral, clay and amorphous components of the sample, their relative abundances, as well as the unit-cell parameters of major crystalline phases (Bish et al., 2014; Morrison et al., 2018a). By May 2019, CheMin had analyzed 3 scooped samples of unconsolidated aeolian sands, as well as 17 drilled samples of mudstones and sandstones spanning all three stratigraphic groups (Achilles et al., 2017; Bish et al., 2013; Bristow et al., 2018; Morris et al., 2016; Rampe et al., 2017; Treiman et al., 2016; Vaniman et al., 2014). CheMin-derived mineral abundances of these samples enable the geochemical compositions acquired by ChemCam to be placed in mineralogical context. Mineralogical information discussed in this study is acquired from the relatively unaltered Stimson bedrock drill samples Big Sky (drilled on sol 1119) and Okoruso (drilled on sol 1332; Morrison et al., 2018b; Yen et al., 2017) in addition to the Gobabeb (sol 1224) and Ogunquit Beach (sol 1832) scooped samples from the Bagnold dune field campaigns 1 and 2 respectively (Fig. 1.A; Achilles et al., 2017; Rampe et al., 2018).

3. Results

3.1. Bulk geochemistry and alteration trends of the Stimson formation

Overall, the Stimson formation has a basaltic geochemical composition with minimal difference between the mean and median compositions and reasonable standard deviations from these means (Table 1 and Fig. 4). Major element oxides largely demonstrate an approximately normal distribution about their peak compositions of 48.0 wt% SiO_2, 0.8 wt% TiO_2, 18.8 wt% FeO_T, 6.0 wt% CaO, and 0.4 wt% K_2O (Fig. 4). Although, the distribution in FeO_T shows a slightly heavy tail towards low compositions (Fig. 4C), and the distributions in SiO_2, TiO_2 and K_2O are slightly skewed towards higher values (Fig. 4A, G & F). Al_2O_3 has a clear bimodal distribution with peaks at 11.8 wt% and 16.9 wt% and, despite the bimodality, the mean and median compositions are approximately equal (Table 1). MgO and Na_2O also have slightly bimodal distributions present in their histograms (Fig. 4D & E) with peaks at 7.1 wt% and 9.2 wt% MgO, and 2.7 wt% and 3.2 wt% Na_2O. These bimodal distributions within Al_2O_3, Na_2O and MgO could

Table 1
Basic statistics of the observation point compositions included in the constrained bulk Stimson formation dataset. Basic statistics include the mean, standard deviation (StDev), minimum (Min), median (Med), maximum (Max), compositional range, and for each major element oxide.

Variable	Mean	StDev	Min	Med	Max	Range
SiO_2	48.6	3.0	42.0	48.1	61.6	19.6
TiO_2	0.9	0.2	0.5	0.9	2.0	1.5
Al_2O_3	13.4	2.9	5.7	13.3	22.5	16.8
FeO_T	18.6	2.4	6.6	19.0	27.1	20.5
MgO	6.9	2.7	0.9	6.8	21.6	20.7
CaO	6.2	1.8	1.6	6.2	11.5	9.9
Na_2O	3.4	0.8	1.7	3.3	8.1	6.4
K_2O	0.6	0.4	0.1	0.5	2.7	2.6

represent subpopulations within the Stimson formation, which are investigated with the cluster analysis.

Density contours for the bulk Stimson formation (Fig. 5) also reflect the compositional spread of data present in the histograms, mean and median statistics. Only Al_2O_3, Na_2O, and MgO show apparent elongation of the contours along their y-axis compared to the concentric circles distributed around the foci for the other major elements (Fig. 5A, D & E). The relatively uniform, concentric distribution of the bulk Stimson contours around the focal composition(s) and lack of their association with alteration feature trends show that the methods used to constrain the dataset appropriately distinguish open-system alteration from bulk rock composition (Fig. 5).

Observation points that have targeted calcium-sulfate veins and cement show strong enrichments in CaO relative to Stimson bedrock similar to the trends outlined for the fluvio-lacustrine groups (Bedford et al., 2019; Nachon et al., 2014), depletions in all other major element oxides, and low total sum of oxides. Alteration halos (shown in Fig. 5 as yellow and red crosses) have a geochemical trend towards high SiO_2 compositions (>80 wt%). The majority of ChemCam halo analyses (yellow crosses) also show low abundances for the other major elements except TiO_2 and some K_2O values reflecting the geochemical trends observed in the Mt. Sharp group halos (Bedford et al., 2019; Frydenvang et al., 2017). Nevertheless, some Stimson halo analyses, which we refer to as High-Al halos in Fig. 5, show an additional trend with an apparent positive correlation for Al_2O_3, Na_2O and K_2O with SiO_2 (red crosses). These high Al_2O_3, Na_2O and K_2O halo analyses trend away from the high Al_2O_3 (~16 wt%) bulk Stimson contour subfocus towards the calculated crystal compositions of Big Sky plagioclase and K feldspar (Fig. 5) and appear to correlate with ChemCam analyzing large, white grains (Fig. E.1 of the Supplementary material).

3.2. Cluster analysis results for bulk Stimson

Results from the multivariate analysis show that five clusters best fit the data for the 8 major element oxide variables used to differentiate them (Table 2). According to the dendrogram (Fig. 6A), Clusters 2 & 3 (similarity level 41.7) are closely linked. Clusters 5 and 1 are the most distinct from Clusters 2, 3, & 4 with a similarity level of 0.0 and 26.0. The Cluster with the greatest proportion of observations is Cluster 3 (155), followed by Cluster 2 (146). Clusters 1 and 5 have the fewest observation points associated with them (4 and 8 respectively).

After the five clusters had been identified, each Stimson analysis was assigned its cluster membership number, and a one-way analysis of variance (ANOVA) was undertaken to calculate the cluster mean compositions and standard deviations that differentiate them in the cluster analysis (Table 2, Fig. 7). Overall, ANOVA results (Table 2, Fig. 6A) suggest that the two largest and most similar clusters - Cluster 2 and Cluster 3 - are differentiated by relative variations in MgO (8.1 ± 2.0 wt % in Cluster 1, 5.9 ± 1.8 wt% in Cluster 2) and Al_2O_3 (11.8 ± 2.2 wt% Cluster 1, 15.0 ± 2.0 wt% Cluster 2) abundances, although some variations in mean composition also exist for SiO_2, Na_2O and K_2O, which are all on average slightly more abundant in Cluster 3. Compositionally, Clusters 2 and 3 are distinguished from the other clusters as they correlate with the subfocal compositions of the Stimson dataset (Fig. 7) and hence are more representative of the average ratios of mixed sandstone components. Some analyses with Cluster 2, 3, and 4 memberships do not belong strongly to their cluster which is reflected in their standard deviations (Table 2 and Fig. 7). However, the association of the Cluster 2 and 3 average compositions with the Stimson formation focal compositions (Fig. 7), and correlation of most Cluster 4 analyses with dark features in the RMI images (Fig. 8C) suggests that these weakly correlated analyses have not significantly skewed the model results. It is therefore likely that the Cluster 2, 3, & 4 averages are still representative of the different components in the Stimson sandstone, particularly in the context of the other statistical analyses (Figs. 6 & 7) and geological observations (Fig. 8).

The other Clusters are even more distinct than the main Clusters 2 & 3 (Fig. 6A). Cluster 1 has the largest concentration of MgO (18.4 ± 2.7 wt%) relative to the other Clusters, and lowest concentrations of Al_2O_3 (7.0 ± 0.9 wt%), Na_2O (2.0 ± 0.2 wt%), and K_2O (0.3 ± 0.2 wt%). Cluster 5 shows the reverse major element abundances to Cluster 1 and 2, showing greater element abundances in SiO_2 (58.0 ± 2.6 wt%), Al_2O_3 (17.7 ± 2.9 wt%), Na_2O (5.9 ± 1.2 wt%) and K_2O (1.6 ± 0.6 wt%), and lower MgO (2.4 ± 1.1 wt%) and FeO_T (9.9 ± 2.5 wt%) concentrations than Cluster 3 (Table 2, Fig. 7). On a plot of Al_2O_3, Na_2O, and K_2O with MgO and FeO_T, Clusters 1 and 5 plot closest to the Big Sky mafic (augite and orthopyroxene) and felsic (plagioclase and K feldspar) calculated mineral compositions respectively (Fig. 7A), while Clusters 1 and 5 appear to represent mineral endmember compositions (Fig. 7A). Cluster 4 does not lie along the same trend of negative correlation between MgO and FeO_T against Al_2O_3, Na_2O, and K_2O as the other Clusters due to its higher SiO_2 and lower CaO abundances relative to Clusters 2 & 3 (Fig. 6A), and overall higher TiO_2 (Fig. 6.A, 7.B & Table 2).

4. Discussion

4.1. Diagenesis and alteration of the Stimson sandstone

The main, open-system aqueous alteration features of the Stimson formation (halos and calcium-sulfate mineral veins) show geochemical compositions that trend away from the Stimson formation bulk density contours indicating that we have successfully removed their influence from the bulk rock geochemistry (Fig. 5). We have also identified a halo alteration trend that extends from the high Al_2O_3 Stimson focus towards the calculated crystalline chemistries of the Big Sky drilled sample plagioclase and potassium feldspars (Morrison et al., 2018b; Yen et al., 2017). This supports the resilience of feldspar minerals to the halo alteration process in comparison to the mafic minerals of the bulk Stimson bedrock (Frydenvang et al., 2017; Hausrath et al., 2018; Yen et al., 2017). The Stimson formation sampled away from these open-system alteration features lacks advanced alteration phases, like phyllosilicates, indicating that the Stimson formation was not altered extensively (Siebach et al., 2017b; Yen et al., 2017). However, the Stimson formation has undergone burial diagenesis through post depositional resurgence of groundwater in order to convert it from a loose, aeolian deposit to the sandstone at the surface today (Banham et al., 2018). Provided the incipient alteration of the Stimson formation occurred in a closed-system, constrained bulk rock geochemistry should be largely representative of the ancient dune deposits before lithification.

Two major mineralogical differences exist between the Stimson formation and the modern dune and soil deposits in Gale crater. CheMin analyses of the Stimson formation did not detect olivine (Yen et al., 2017), but showed that Stimson contains 16.2–18.4 wt% iron-oxide minerals compared to the Bagnold dunes that instead have 3.0–4.8 wt % iron-oxides and 25.8–18.2 wt% olivine (Achilles et al., 2017; Rampe et al., 2018). Reactive transport aqueous alteration models of the

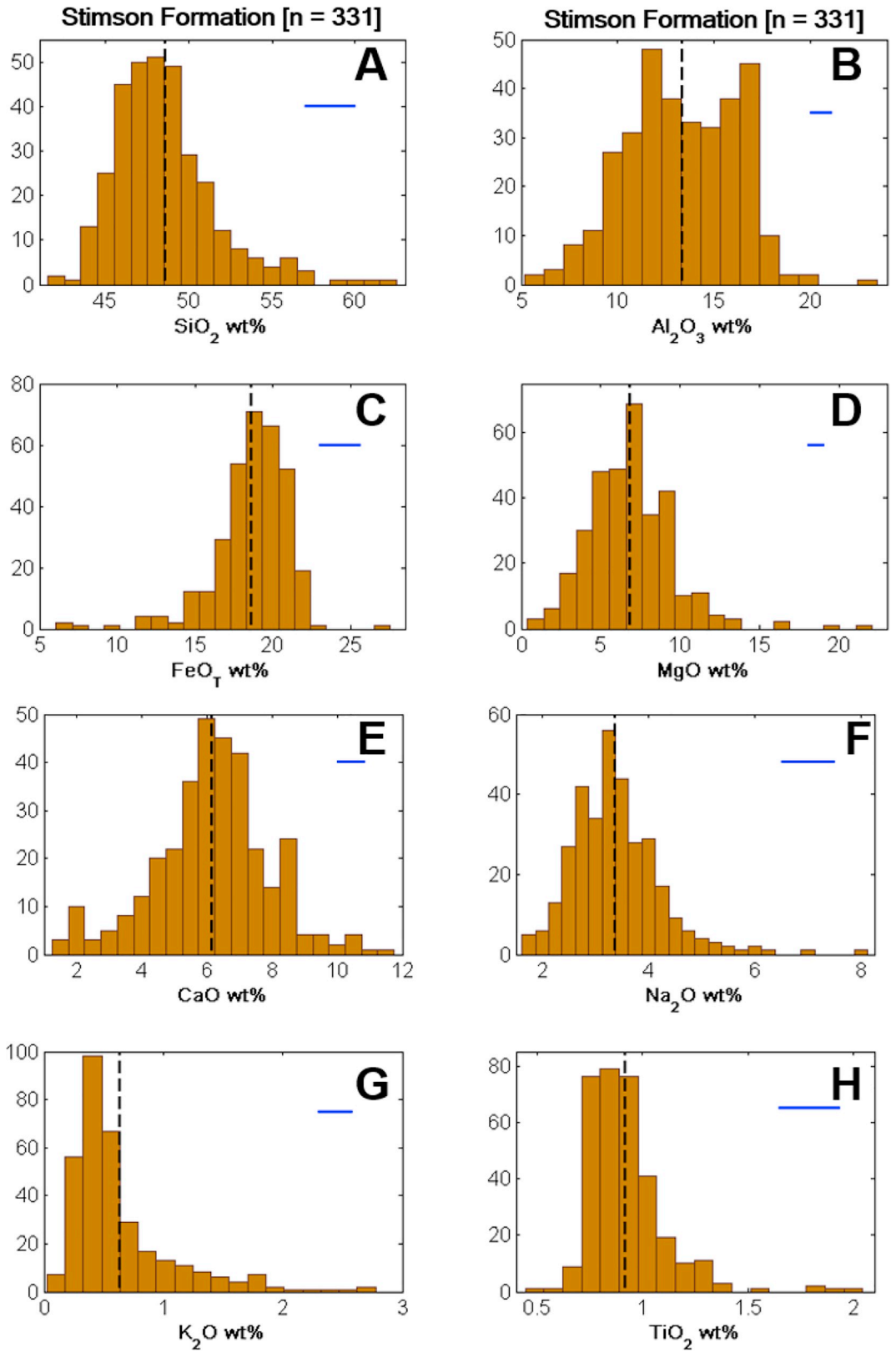

Fig. 4. Major element histograms of Stimson analyses within 95–105% sum of oxides, and excluding observation points taken >4 m from the rover or that had analyzed obvious diagenetic features. Mean compositions (dashed vertical line) and 1σ precision (horizontal blue line) are also shown. (For interpretation of the references to colour in this figure legend, the reader is referred to the web version of this article.)

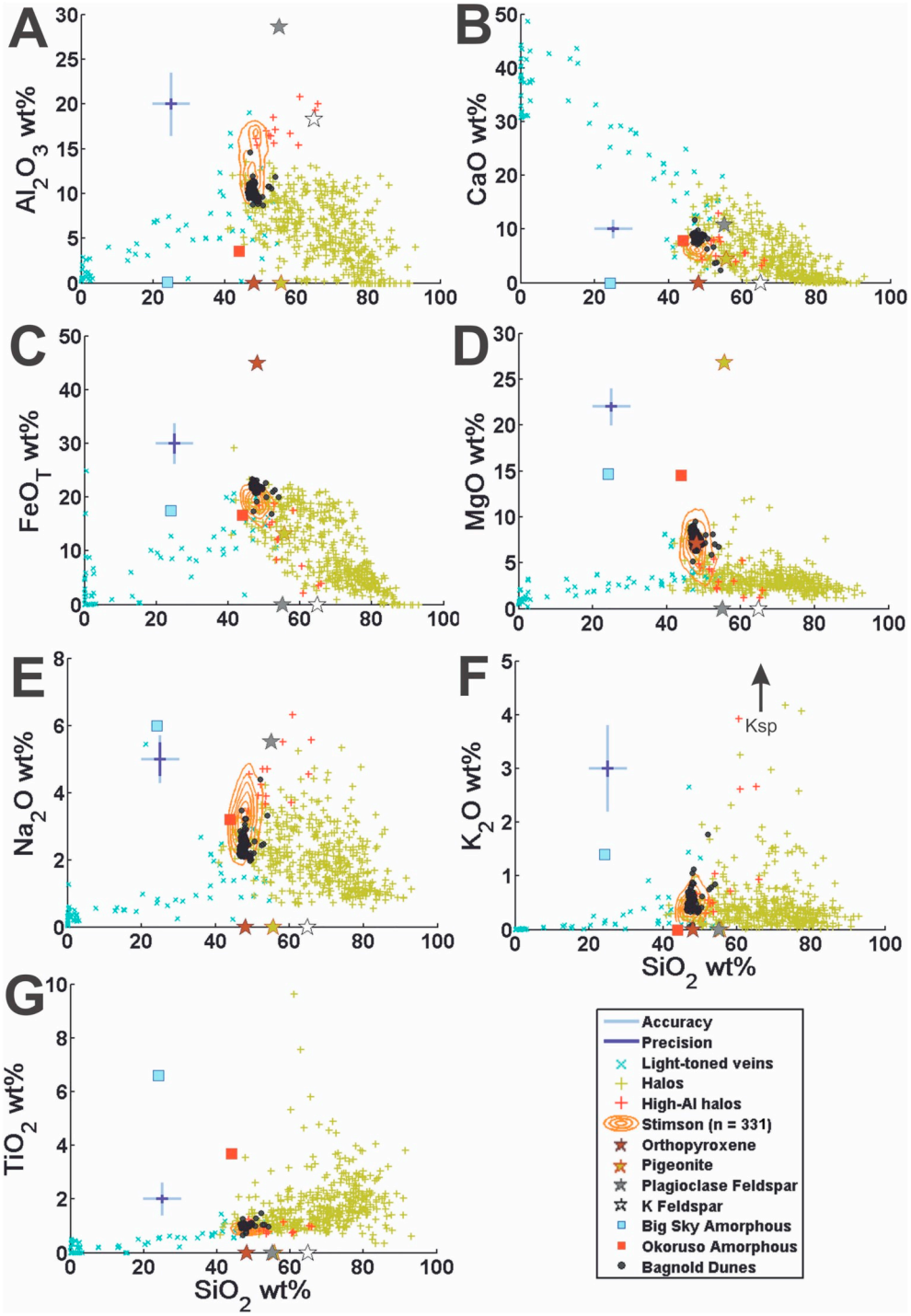

Fig. 5. Density contour Harker plots of the constrained Stimson dataset for each major element against SiO_2 with a level step of 0.001, smoothing factor 30 and bin size 50. Alteration feature trends are shown as yellow and red crosses for the light-toned halos, and light blue crosses for the Ca-sulfate veins. Data also included are the Big Sky plagioclase feldspar, K-feldspar, pigeonite and orthopyroxene mineral compositions from Morrison et al. (2018b) shown as stars, and the Big Sky and Okoruso amorphous component best estimate from Morrison et al. (2018b) shown as squares. The light and dark blue crosses show the ChemCam instrument accuracy and precision respectively to 1σ. K fekdspar in F) illustrates the direction of the CheMin derived K-feldspar composition from Morrison et al. (2018b) which contains16.9 wt% K_2O. Black circles are the Bagnold dune ChemCam observation point analyses. (For interpretation of the references to colour in this figure legend, the reader is referred to the web version of this article.)

Stimson formation have shown that the prevalent iron-oxide cement and high abundance of MgO (~15 wt% APXS, Big Sky and Okoruso; Morrison et al., 2018b) in the amorphous component is likely the product of olivine subjected to burial diagenesis at 1 °C and pH 6–8 (Hausrath et al., 2018). This diagenesis makes it likely that the high MgO and FeO_T Clusters 1 and 2 could relate to ChemCam points that have sampled a greater proportion of iron-oxide and MgO-bearing amorphous sandstone cement that constitutes on average 31 wt% of the Big Sky and Okoruso drilled Stimson samples (Morrison et al., 2018b). Cluster 2 also has high abundances of MgO suggesting a possible influence of the amorphous component, but MgO compositions in Cluster 2 (8.1 ± 2.0 wt%) are more similar in composition to the CheMin derived crystalline component that includes orthopyroxene and pigeonite (6.2–7.0 wt% MgO, Morrison et al., 2018b). ChemCam RMI images of targets with Cluster 1 and 2 memberships support that Clusters 1 and 2 may relate to fine-grained mafic minerals or dark iron-oxide and amorphous-bearing sandstone cement as these targets are generally fine grained, dark-toned, and have not sampled any obvious light-toned mineral grains (Fig. 8A). In particular, Cluster 1 consists of four isolated observation points that are all situated in different ChemCam targets in the Emerson plateau, with two Cluster 1 targets - Mission Creek and Chamberlain - analyzed on sol 1099 indicating that there may have been larger pockets of sandstone cement in this area.

Provided the diagenesis that cemented the Stimson sandstone was

Table 2
Mean compositions of the 5 clusters identified in the cluster analysis with the standard deviation, number of observations within each cluster (N), F-values (F) and *p*-values (*p*) derived from the F-test statistic[1]. Box shading refers to relative abundances of the different major element oxides where yellow is high and dark green is low.

Cluster	SiO_2 (wt%)	TiO_2 (wt%)	Al_2O_3 (wt%)	FeO_T (wt%)	MgO (wt%)	CaO (wt%)	Na_2O (wt%)	K_2O (wt%)	N
1	47.5 ± 1.6	0.8 ± 0.1	7.0 ± 0.9	20.1 ± 0.8	18.4 ± 2.7	3.1 ± 1.6	2.0 ± 0.2	0.3 ± 0.2	4
2	47.1 ± 2.1	0.9 ± 0.2	11.8 ± 2.2	19.6 ± 1.7	8.1 ± 2.0	6.5 ± 1.7	2.9 ± 0.5	0.4 ± 0.2	146
3	49.0 ± 2.2	0.9 ± 0.1	15.0 ± 2.0	18.0 ± 1.9	5.9 ± 1.8	6.3 ± 1.6	3.8 ± 0.6	0.8 ± 0.5	155
4	52.7 ± 4.1	1.3 ± 0.4	10.6 ± 2.4	19.9 ± 1.3	4.5 ± 1.7	4.8 ± 1.8	3.2 ± 0.6	0.6 ± 0.2	18
5	58.0 ± 2.6	0.9 ± 0.2	17.7 ± 2.9	9.9 ± 2.5	2.4 ± 1.1	3.2 ± 1.0	5.9 ± 1.2	1.6 ± 0.6	8
F	43.6	4.6	93.1	42.0	73.1	21.6	77.2	23.9	
P	0.0000	0.0004	0.0000	0.0000	0.0000	0.0000	0.0000	0.0000	

[1]*p*-Values were generated using one-way ANOVA on the data assigned to each cluster membership in order to determine statistical significance from one another. Unequal variance was assumed for the ANOVA analysis.

isochemical, it is still possible to use MgO and FeO_T as a proxy for the mafic minerals that were originally deposited in the Stimson dune field as the bulk chemistry will not have changed. The first evidence to support the isochemical nature of the Stimson sandstone cement is shown by the equivalent composition of concretionary and non-concretionary sandstone in the Stimson formation according to both APXS geochemical data (Banham et al., 2018; Siebach et al., 2017b), and the ChemCam data reported here (Appendix B). Concretions form due to the preferential cementation of the sandstone, making them more erosion resistant when exposed at the surface (Banham et al., 2018; Chan et al., 2012; Potter-McIntyre et al., 2014; Potter et al., 2011). As these more cemented parts of the sandstone are not geochemically distinct from the non-concretionary cement, they can be considered to have formed isochemically with reactants sourced locally from the ferromagnesian minerals (Banham et al., 2018; Hausrath et al., 2018; Potter-McIntyre et al., 2014; Siebach et al., 2017b). Next, the absence of clay minerals in CheMin analyses of Stimson sandstone suggests that the diagenesis was not pervasive enough to form phyllosilicates and shows that it did not occur in an open-system (Yen et al., 2017), hence, the overall geochemistry of the initial sand deposit is likely to have been maintained. Finally, the focal composition of bulk Stimson MgO is equivalent to the MgO concentrations of the Bagnold dune analyses (Fig. 5.D) and when Bagnold dune olivine is included in a plot of major elements associated with felsic minerals plotted against those associated with mafic minerals (Fig. 7A), the linear regression line plots near perfectly through the center of the Stimson mafic and Bagnold olivine compositions suggesting that they both contained olivine. All these factors indicate that the Stimson sandstone cement formed in a closed-system and as such, we continue to use MgO and FeO_T as a proxy for the mafic minerals that were initially deposited in the original dune sands.

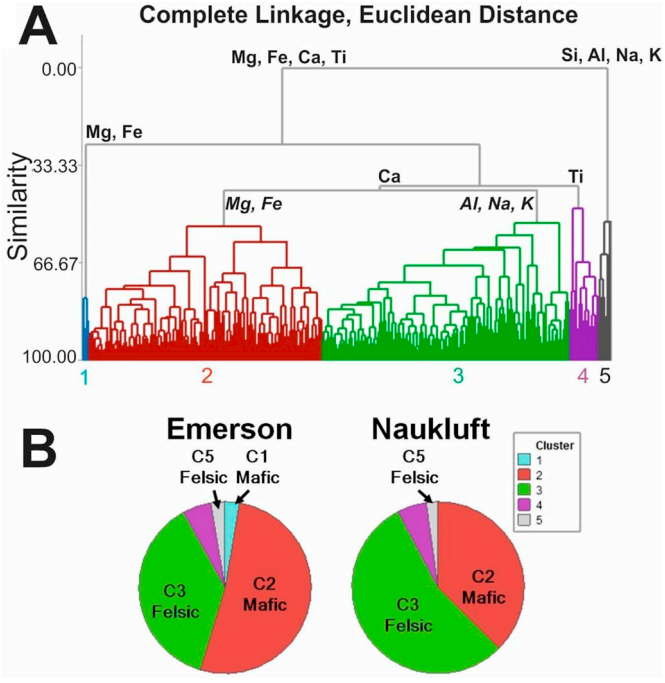

Fig. 6. A) A dendrogram derived from the Cluster analysis on bulk Stimson observation points. According to the change in similarity levels, 5 clusters were derived from this formation. Blue = Cluster 1, red = Cluster 2, green = Cluster 3, pink = Cluster 4, grey = Cluster 5. The geochemical variations that define the different clusters are shown at the branching points with italicised major elements for Clusters 2 and 3 indicating relative major element differences between these two clusters. B) Pie charts showing the proportion of each cluster between the Emerson and Naukluft Plateaus. (For interpretation of the references to colour in this figure legend, the reader is referred to the web version of this article.)

4.2. *Constraining the mineral sorting regime in the Stimson formation with clusters 1, 2, 3, & 5*

Clusters 2 and 3 are the most similar to the bulk Stimson composition and are distinguished from one another by their relative concentrations of Al_2O_3, Na_2O, and K_2O compared to MgO (Table 2, Fig. 7A). This is similar to the geochemical differences between Clusters 1 and 5, with Cluster 1 showing the highest abundance of MgO, and Cluster 5 the highest abundances of Al_2O_3, Na_2O, and K_2O (Table 2, Fig. 7A). Hence, Clusters 1 and 5 appear to be closer to endmember compositions than Clusters 2 and 3, which are instead more representative of the subpopulations in the Stimson formation that are the cause of the bimodal distributions for Al_2O_3, MgO and Na_2O (Fig. 4B, D, and F).

According to calculated CheMin mineral compositions of the Stimson formation drilled samples Big Sky and Okoruso, Al_2O_3 is determined by the proportion of the felsic minerals plagioclase and K-feldspar, MgO is influenced by the abundances of the mafic minerals pigeonite and orthopyroxene, and previously by olivine (Hausrath et al., 2018), Na_2O is located within plagioclase feldspar, and K_2O within K-feldspar (Morrison et al., 2018b). When a regression line is calculated for bulk Stimson data using major element oxides that solely constitute plagioclase feldspar and K feldspar (Al_2O_3, Na_2O and K_2O) against those only found in mafic minerals (MgO and FeO_T) a straight line ($R^2 = 56.4\%$; $p < 0.001$) is plotted through the Stimson focus (Fig. 7.A) and plots between the Big Sky mafic and felsic mineral compositions derived by Morrison et al. (2018b). Clusters 1, 2, 3, and 5 lie within error of this line (Fig. 7A). Clusters 2 and 3 are also situated about the focal compositions of the Stimson sandstone, which supports that Clusters 1 and 5 are closest in composition to mineral endmembers, with Clusters 2 and 3 correlating to analyses that have targeted an average Stimson mixing proportion of respective mafic and felsic mineral populations (Fig. 7A). These clusters

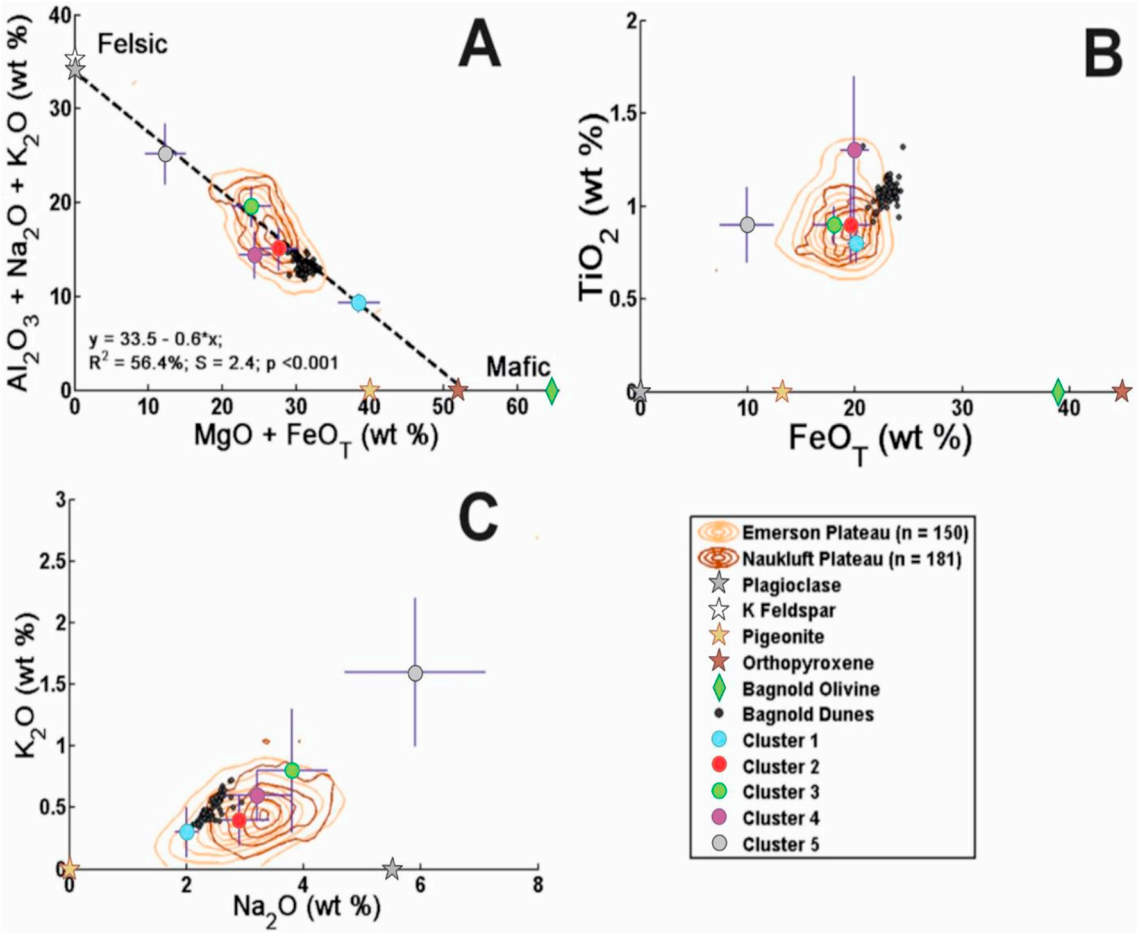

Fig. 7. Density contour and scatter plots for the constrained Emerson Plateau (orange contours) and Naukluft Plateau (dark brown contours), cluster average compositions (circles), and CheMin-derived Big Sky drilled sample mineral chemistry (stars; Yen et al., 2017; Morrison et al., 2018b). The Big Sky mineral compositions were selected as they show the least evidence of alteration (Yen et al., 2017). A) Also shows a modelled linear regression line for data with mafic and felsic cluster memberships that shows statistical significance according to $p < 0.05$. (For interpretation of the references to colour in this figure legend, the reader is referred to the web version of this article.)

with an apparent negative correlation between Al_2O_3, Na_2O, and K_2O versus MgO and FeO_T are similar to the mafic and felsic clusters determined from several cluster analysis studies of ChemCam data from the inactive Aeolus Palus soils in Gale crater (Cousin et al., 2015; Meslin et al., 2013). Therefore, it is probable that the Clusters from the Stimson formation ChemCam data are also representative of the different proportions of mafic and felsic minerals that existed in the previously deposited Stimson dune field and can be used to understand the effects of sediment transport on bulk Stimson geochemistry.

When Stimson density contours are divided into the Emerson and Naukluft plateaus (Fig. 7), the Emerson plateau shows a distribution and bulk composition that extends to higher MgO and FeO_T, and lower Al_2O_3, Na_2O and K_2O compared to the Naukluft plateau (Fig. 7). Although the bulk compositional differences are small between Stimson localities, the geochemical variation between localities are shown to be statistically significant with two-way equivalence tests for Al_2O_3, MgO, CaO, and K_2O (see Table F.1 of Supplementary information). Overall, the Emerson plateau density contours on the mafic-felsic mineral sorting plot show a larger spread in compositional data than the Naukluft plateau contours, extending towards more mafic compositions (Fig. 7A). Alternatively, the Naukluft plateau density contours are fewer in number denoting a lower spread in data with a focus extending more to the felsic Clusters 3 and 5. The distribution of clusters between the two localities also shows that the Emerson plateau has a higher proportion of points within the mafic cluster memberships (Clusters 1 and 2) compared to Stimson analyzed at the Naukluft plateau which in turn has a much greater proportion of points associated with felsic clusters (Clusters 3 and 6, see Fig. 6.B). Further support for the mafic classification of Clusters 1 & 2 and felsic classification of Clusters 3 & 5 is provided by the target RMI images (Fig. 8). Targets with Cluster 1 & 2 classifications have fewer coarse, light toned mineral grains in them (Fig. 8A) compared to targets with Cluster 3 and 5 classifications that show several, often coarse (>1 mm) light-toned mineral grains (Fig. 8B).

Mineral sorting within the dunes themselves and deposition across different geological time periods were considered as possible causes of mafic-felsic geochemical variation for the Emerson and Naukluft plateaus. On Mars, the proportion of olivine/feldspar is shown to vary from ripple and dune troughs to crests with crests being more enriched in the coarser mafic material relative to the troughs (Johnson et al., 2017; Lapotre et al., 2017; O'Connell-Cooper et al., 2018, 2017). A plot of mafic and felsic ChemCam clusters against height above the unconformity does not show a correlation of mafic-felsic proportions with position in the dune outcrop (Appendix Fig. G.1). Dune crests are also rarely preserved in the geological record (Banham et al., 2018; Kocurek, 1991; Nichols, 2009), hence, ChemCam has successively sampled the lower portion of the ancient dunes avoiding the bias associated with mineral sorting within the dunes themselves. Therefore, the mafic-felsic mineral proportions are clearly associated with locality rather than elevation or position in the dune. The similarity between the minerals that constitute the Stimson formation across both plateaus and lack of sedimentological

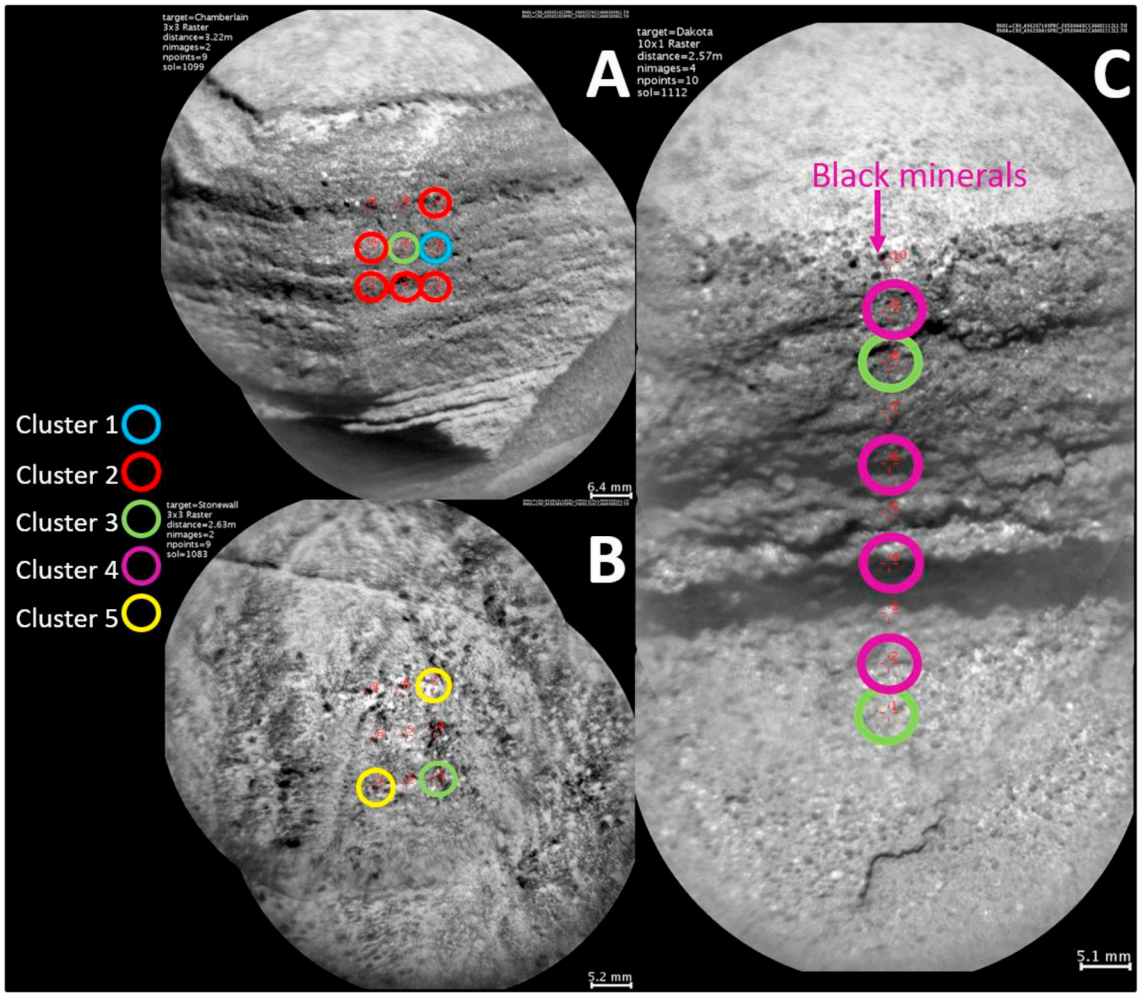

Fig. 8. ChemCam RMI images of targets with different proportions of cluster memberships. A) Target Chamberlain (sol 1099) from the Emerson Plateau is a dark sandstone with few coarse, light-toned minerals and mostly Cluster 1 & 2 memberships. B) Target Stonewall (sol 1083) from the Emerson Plateau. This target has abundant, coarse grained felsic minerals and only Cluster 3 & 5 memberships. C) Target Dakota (sol 1112) from the Naukluft Plateau. This target has several high-Ti Cluster 4 memberships and contains abundant black minerals that are uncommon in targets without a Cluster 4 membership, in addition to coarse, felsic grains.

features that indicate a period of aeolian deflation i.e., super surfaces (Banham et al., 2018; Kocurek, 1988), also indicates that Stimson was deposited during a single period of aeolian accumulation (Banham et al., 2018; Yen et al., 2017). As such, it is highly unlikely that mafic-felsic geochemical variation occurred as a result of either mineral sorting within dunes or a change in stratigraphic position. We therefore hypothesize that the ancient net sediment transport direction can be inferred according to the mafic-felsic mineral sorting regime across the Stimson formation, particularly if the sediments were derived from a line or point source with a single source geometry (Ewing and Kocurek, 2010).

The aeolian mineral sorting regime determined from the unconsolidated soil deposits in Gale crater and Mars-analog basaltic aeolian dunes in Iceland both show that coarse-grained felsic minerals are more abundant closer to the sediment source compared to the often finer mafic minerals such as olivine and pyroxene that are transported further in the system (Baratoux et al., 2011; Cousin et al., 2015; Mangold et al., 2011; Meslin et al., 2013; Mountney and Russell, 2004). The preferential transportation of mafic mineral grains in aeolian environments occurs as their rounder shape and finer grain size made them more efficient at saltation compared to the elongate feldspar grains (Baratoux et al., 2011; Mangold et al., 2011; Mountney and Russell, 2004). Due to the increased abundance of mafic minerals in the finer portion of basaltic sediments that are transported further in aeolian processes, aeolian sand further from the source is richer in MgO and FeO, but has a lower abundance of Al_2O_3, Na_2O and K_2O (Baratoux et al., 2011; Cousin et al., 2015; Mangold et al., 2011). This mineral sorting regime and compositional characteristic is also identified in the Bagnold dunes in Gale crater (Lapotre et al., 2017; Rampe et al., 2018), although, the Bagnold dunes appear to be either better sorted than the Gale crater soils or derived from a more olivine-phyric source region due to their uniform geochemistry, concentration of olivine, and absence of coarse, felsic grains at the dune crests (Cousin et al., 2017; Johnson et al., 2017; O'Connell-Cooper et al., 2018). The lower chemical weathering rates for present-day Mars may also promote the preservation of relatively coarse olivine grains in currently active aeolian systems such as the Bagnold dunes. Whereas, soil deposits may in comparison have higher hydration signals due to the presence of a < 100 μm fine fraction that could relate to alteration products present in the Martian dust (Cousin et al., 2017, 2015; Gabriel et al., 2018).

In the Stimson formation, coarse, light-toned mineral grains ~1.5 mm in size have been identified in images across the Emerson and Naukluft plateaus (e.g., Fig. 8), particularly in Naukluft plateau targets, showing that feldspar is present in the coarser grain size fractions (>250 μm) of the ancient Stimson dune field. Furthermore, the proportion of felsic Clusters 3 and 5 is greater in the Naukluft plateau relative to the Emerson plateau which is instead more abundant in mafic Clusters 1 and 2 (Fig. 6B). According to this mineral sorting regime, the greater

proportion of felsic clusters in the Naukluft plateau relative to the Emerson plateau suggests that the sand deposited at the Naukluft plateau was closer to the sediment source. With the mafic-felsic aeolian mineral sorting regime taken into account, this would imply a wind regime with a net resultant SW–NE sediment transport direction to concentrate more coarse, felsic grains in the Naukluft plateau relative to the Emerson plateau. This net resultant wind direction is consistent with the wind direction derived from the cross-lamination dip-azimuths within the Stimson formation at the Emerson plateau by Banham et al. (2018). However, the net resultant wind direction for the Stimson formation is opposite to that of the modern Bagnold dune deposits which instead migrate in a NE–SW transport direction (Banham et al., 2018; Bridges et al., 2017; Ewing et al., 2017; Lapotre et al., 2017).

4.3. The cluster 4 TiO_2-bearing sandstone component

Cluster 4 analyses are enriched in TiO_2 (1.3 ± 0.4 wt%) relative to bulk Stimson (Fig. 7.B), and constitute a similar proportion of the observation points at both localities (~5% at the Emerson and Naukluft plateaus; Fig. 6). Cluster 4 plots away from the mafic-felsic trendline (Fig. 7.A) suggesting it is influenced by a high-TiO_2 endmember different from the mafic and felsic minerals controlling the bulk geochemistry of most data points. We propose three possible explanations for high TiO_2 concentrations: contamination from the silica-rich halos (Fig. 5.G), analysis of detrital Ti-bearing mineral grains (e.g., ilmenite) entrained within the sand dunes, or a TiO_2-rich cement/amorphous component (Fig. 5.G). None of the observation points that constitute the Cluster 4 group show any association with these alteration halo features in the Mastcam, Navcam, or RMI images. Instead, Cluster 4 analyses are distributed across 10 ChemCam targets between both the Emerson and Naukluft plateaus, and appear to have targeted either dark-toned sandstone cement, or in some cases such as Dakota (sol 1112, Fig. 8A), they have targeted dark inclusions in the sandstone indicating a possible mineral or cement component. Ti-bearing minerals such as ilmenite were detected at 1.4 wt% abundance in the Rocknest sand shadow (Bish et al., 2013; Morrison et al., 2018b), showing that it is possible for Ti-rich minerals to be entrained within sand deposits on Mars. Although ilmenite was not present above the limit of detection for CheMin in the Stimson formation (Yen et al., 2017), it is not an impossible component given the limited number of Stimson CheMin analyses. Furthermore, the dark-toned, possibly tetragonal mineral grains in some ChemCam targets with Cluster 4 memberships could be candidate ilmenite grains (Fig. 8C). Alternatively, another probable source for Cluster 4 analyses is from the Stimson amorphous component which has been calculated to contain the majority of the TiO_2 (14–25 wt %) within both Big Sky and Okoruso drilled samples (Morrison et al., 2018b; Yen et al., 2017). Microcrystalline Ti-rich minerals such as titanomagnetite, brookite or anatase have been identified in terrestrial sandstone cements that contain iron-oxide cement (Morad and Aldahan, 1982; Pe-Piper et al., 2011). These Ti-rich cement components form during the diagenesis of Ti-bearing igneous minerals such as ilmenite or pyroxene (Morad and Aldahan, 1982; Pe-Piper et al., 2011) and may therefore also be the cause of Cluster 4 analyses.

4.4. Source regions

4.4.1. Changes in source between the ancient and modern sedimentary deposits

Mineral sorting has been shown to have a local effect on geochemical composition in relation to Al_2O_3, MgO, Na_2O, and K_2O between the Emerson and Naukluft plateaus (Fig. 7.A). However, this effect is small according to the relative differences in composition calculated for the equivalence tests (Appendix Table F.1) and should not have affected the overall bulk chemical composition of the Stimson formation provided analyses from both plateaus are taken into account to average out the relative enrichments and depletions of minerals between the localities.

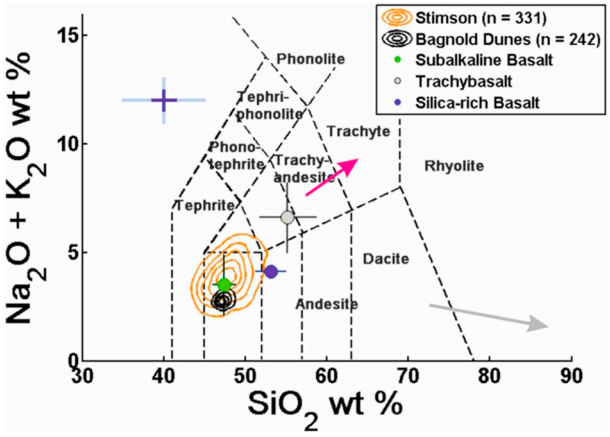

Fig. 9. A total alkali versus silica (TAS) plot (Irvine and Baragar, 1971) used to classify igneous rocks and give a preliminary understanding on sediment source region if alteration and mineral sorting processes are shown to have a minimal effect on sediment geochemistry. Stimson contour level step = 0.001, bin size = 50 and smoothing factor = 30. Bagnold dune contour level step = 0.003, bin size = 50 and smoothing factor = 30. Known sediment endmembers with 1σ error derived by Bedford et al. (2019) are shown as green (subalkaline basalt), grey (trachybasalt) and dark blue (silica-rich basalt) circles. Endmembers inferred from unique minerals identified in Gale's sediment succession are shown as pink (trachyte, cf. Treiman et al., 2016) and grey (rhyolite, cf. Morris et al., 2016) arrows. (For interpretation of the references to colour in this figure legend, the reader is referred to the web version of this article.)

Hence, analyzing the bulk Stimson geochemistry in relation to the modern dune deposits and preserved fluvio-lacustrine units can provide an indicator of how bulk compositions of igneous source regions have changed since a river-lake environment deposited the Bradbury and Mt. Sharp Groups in Gale crater (see Bedford et al., 2019), to the dry aeolian climate on the surface today (Banham et al., 2018).

When comparing the bulk geochemical composition of the modern dunes in Gale crater to the Stimson formation, normalized Bagnold dune analyses show similar SiO_2, MgO, K_2O and TiO_2 with slightly lower Al_2O_3 and Na_2O, and higher CaO and FeO_T compared to bulk Stimson (Figs. 5 & 7). In a total alkali versus silica plot (Fig. 9), both the ancient and modern dune deposits are situated comfortably within the subalkaline basalt field with the Stimson focus at 47.7 ± 0.1 wt% SiO_2 and 3.7 ± 0.04 wt% alkalis and the Bagnold dune focus at 47.0 ± 0.1 wt% SiO_2 and 2.8 ± 0.01 wt% alkalis. The geochemistry of the ancient and modern dune deposits therefore suggests a predominately basaltic origin, although there are differences in bulk alkali compositions. These variations all relate to different minerals and mineral compositions that most likely reflect variation in source region (e.g., Gobabeb has a high abundance of augite and no orthopyroxene compared to Stimson which has no augite but abundant orthopyroxene and pigeonite; Achilles et al., 2017; Morrison et al., 2018b; Rampe et al., 2018). This difference in sediment source regions, also hypothesized by Achilles et al. (2017) based on the mineralogical differences, would be expected given the different geological time under which the deposits formed and the change in net sediment transport directions from the deposition of the ancient and modern dune deposits discussed above. This shows that the availability of different sediment sources changed with time which owing to either the evolution of Gale crater's topographic profile or the change in wind regime transporting material from a different source area.

The Stimson formation plotting closer towards the felsic corner of the mafic-felsic mineral sorting plot compared to the modern Bagnold dunes (Fig. 7A) suggests that i) that chemical weathering rates were higher in the past limiting the preservation of olivine grains in the system, ii) the Stimson dunes were sourced from more local material to generate the higher abundance of coarse, felsic minerals, or iii) the Stimson dunes

were derived from a more plagioclase-phyric source region. Chemical weathering rates are unlikely to have been the main cause of geochemical variation between the Bagnold dunes and Stimson formation due to the similar MgO and SiO_2 concentrations of the Stimson formation to the Bagnold dunes (Fig. 5D), the mafic-felsic linear regression model of Stimson and Bagnold dune ChemCam data plotting between the calculated crystal chemistries of the Gobabeb olivine and Stimson pyroxenes (Fig. 7A), and hydrous alteration models suggesting that olivine is a likely source of the Stimson sandstone cement (Hausrath et al., 2018). Furthermore, chemical weathering would be negligible in the arid environment required for dry-aeolian dune formation, so we hypothesize that olivine was also transported in the ancient dunes similar to the Bagnold dunes. Due to the Stimson formation having an opposite net sediment transport direction to the modern Bagnold dunes, and due to the differences in geochemistry and mineralogy between the Bagnold dunes and Stimson formation, we hypothesize that different sediment sources are a more likely explanation for the mineralogical and compositional differences between these deposits. An orbital study of the modern aeolian processes and dune morphologies in Gale crater by Hobbs et al. (2010) postulates that the aeolian dunes at the base of Mt. Sharp - including the Bagnold dunes - are sourced from low-albedo areas to the North and North-West outside of Gale crater. This would suggest that the sediments of the Bagnold dunes have been transported over distances of up to 200 km (Hobbs et al., 2010) and are therefore likely to be well-sorted aeolian deposits. Given the overall coarser average grain size of the Stimson formation (406 μm) relative to the Bagnold dunes (120 μm) (Banham et al., 2018), the opposite transport direction determined from sedimentological features (Banham et al., 2018) and compositional trends in ChemCam data, the greater compositional variation of the Stimson formation relative to the Bagnold dunes, and the possible presence of heavy ilmenite grains in the Stimson formation based on Cluster 4 analyses (Figs. 7B & 8C), it is likely that the sediments that now comprise the Stimson formation experienced limited aeolian transport compared to sediments in the Bagnold dunes. This indicates a relatively local source for the Stimson formation. Another factor hypothesized by Banham et al. (2018) to contribute to an overall coarser grain size in the Stimson formation compared to the modern Bagonld dunes is that the atmosphere may have been thicker when the Stimson formation was deposited. A thicker atmosphere would have enabled the transportation of coarser grains over longer distances. However, on the basis that this study has been able to identify a geochemical effect of mineral sorting between the localities that are <1 km apart, a relatively local source is still preferred for the Stimson formation and is discussed further below.

4.4.2. *A common source region between the fluvio-lacustrine groups and the Stimson formation*

When comparing the bulk geochemical compositions of the main sedimentary units in Gale crater, the Stimson formation presents distinct differences to the Mt. Sharp group as well as the modern Bagnold dunes (Figs. 5, 10). In contrast, the Stimson formation and Bradbury group are similar to each other with notably similar focal compositions for SiO_2 (~47 wt%), FeO_T (~20 wt%), MgO (~7.5 wt%), Na_2O (~3 wt%), K_2O (0.5 wt%) and TiO_2 (0.9 wt%) (Fig. 10). This similarity in bulk geochemistry between the Bradbury group and Stimson formation has been noted before between ChemCam measurements of the Big Sky drilled sample and Bradbury group rocks (Gasnault et al., 2019) and could relate to a common, long-lived source region. The main geochemical differences between the Stimson formation and Bradbury group are the larger spread in compositional range for the Bradbury group, particularly for Al_2O_3, CaO, FeO_T, K_2O and TiO_2, and the focal compositions for Al_2O_3 which is a little higher for Stimson (12.8 ± 0.3 wt %) compared to the Bradbury group (10.6 ± 1.2 wt%). The greater range in contour compositions for the Bradbury group may result from at least three distinct sediment source regions – subalkaline basalt, trachybasalt, and a sanidine-rich trachyte – contributing to its sedimentary record (Bedford et al., 2019; Edwards et al., 2017; Siebach et al., 2017a; Treiman et al., 2016). The Stimson formation focal compositions correlate with the geochemistry of the subalkaline basalt source region, which is the main source region of the Bradbury group sandstone and mudstone, but it shows no obvious influence of the trachybasaltic sediment source or the sanidine-rich sediment source according to the smaller degree of geochemical variation (Fig. 10). Previous studies (Bedford et al., 2019; Edwards et al., 2017; Siebach et al., 2017a) have suggested that the dominant sediment source region of the Bradbury group was a subalkaline basalt similar to the Adirondack Class subaerial lavas analyzed in Gusev crater (McSween et al., 2006) and the Gale crater basaltic igneous float and clasts studied by Edwards et al. (2017) and Cousin et al. (2017). As both the Stimson formation and Bradbury group focal compositions are situated at the subalkaline basalt endmember, this suggests that they shared a dominant source region. The Bradbury group is hypothesized to have been eroded and transported into Gale crater from the Northern crater rim according to geomorphic and sedimentary features (Buz et al., 2017; Deit et al., 2013; Grotzinger et al., 2015). Spectra acquired from the Compact Reconnaissance Imaging Spectrometer for Mars on-board the orbiting Mars Reconnaissance Orbiter show that the olivine-bearing bedrock of the Northern crater rim and walls, which is the likely provenance of the Bradbury group sediments, extends around Gale crater (Buz et al., 2017). As a result, it is possible that the Stimson formation may have also been sourced from the walls and rim of the crater despite the Stimson formation having been transported from the southwest of its current location (Banham et al., 2018) and the Bradbury group transported from the north.

Alternatively, aeolian processes are efficient at eroding underlying bedrock and incorporating the sediments into its bedforms during sediment recycling (Cardenas et al., 2019; Dott, Jr, 2003; Garzanti et al., 2013; Swanson et al., 2019). A current hypothesis for the formation of Mt. Sharp involves wind excavating Mt. Sharp from the sediments that had originally infilled Gale crater (Anderson, 2010; Day et al., 2016; Grotzinger et al., 2015). If this is indeed how Mt. Sharp formed, it is plausible that some of the aeolian deposits in Gale crater contain sediments derived from the reworking of previously deposited sedimentary material. Notably, aeolian deposits in Gusev crater have shown local variations in chemistry relating to the surrounding bedrock (Ming et al., 2008). Locally derived sediments have also been shown to contribute to the modern aeolian deposits of Gale as either large grains of local material in soils (Bish et al., 2013; Cousin et al., 2015; Meslin et al., 2013), calcium-sulfate and mudstone clasts in sand dunes (Achilles et al., 2017), or Mt. Sharp group mudstone intraclasts incorporated into the base of the Stimson formation (Banham et al., 2018; Newsom et al., 2018). As the Mt. Sharp group that underlies the Stimson formation is a mudstone, it is unlikely that its fine grain size would be preserved in the ancient Stimson sand dunes as grains smaller than fine sand are winnowed away in dry-aeolian environments (Banham et al., 2018). The majority of the fluvial sandstones in the Bradbury group are basaltic in composition (Bedford et al., 2019; Siebach et al., 2017a), and this, along with the basaltic mudstone in the Bradbury group is what defines the basaltic focal composition in the contour plot (Fig. 10; Bedford et al., 2019). Therefore, the Stimson dunes may be compositionally similar to the Bradbury group due to the Stimson dunes preferentially preserving the coarser grains of a similar basaltic sandstone unit instead of being derived from similar source regions.

Basaltic sandstone similar to the Bradbury group situated further SW of the Curiosity rover traverse is possible given that previous orbital mapping of the crater floor in the NW of Gale crater has placed it within the same unit (Hummocky Plains by Anderson, 2010, or Crater Floor 1 unit by Le Deit et al., 2013), however, several mineralogical differences exist between the Bradbury group and Stimson formation that cannot be explained by the winnowing of fine material. The results of this study and studies of aqueous alteration in the Stimson formation suggests that the Stimson formation once contained abundant olivine comparable to that detected in the active Bagnold dune deposits (Hausrath et al.,

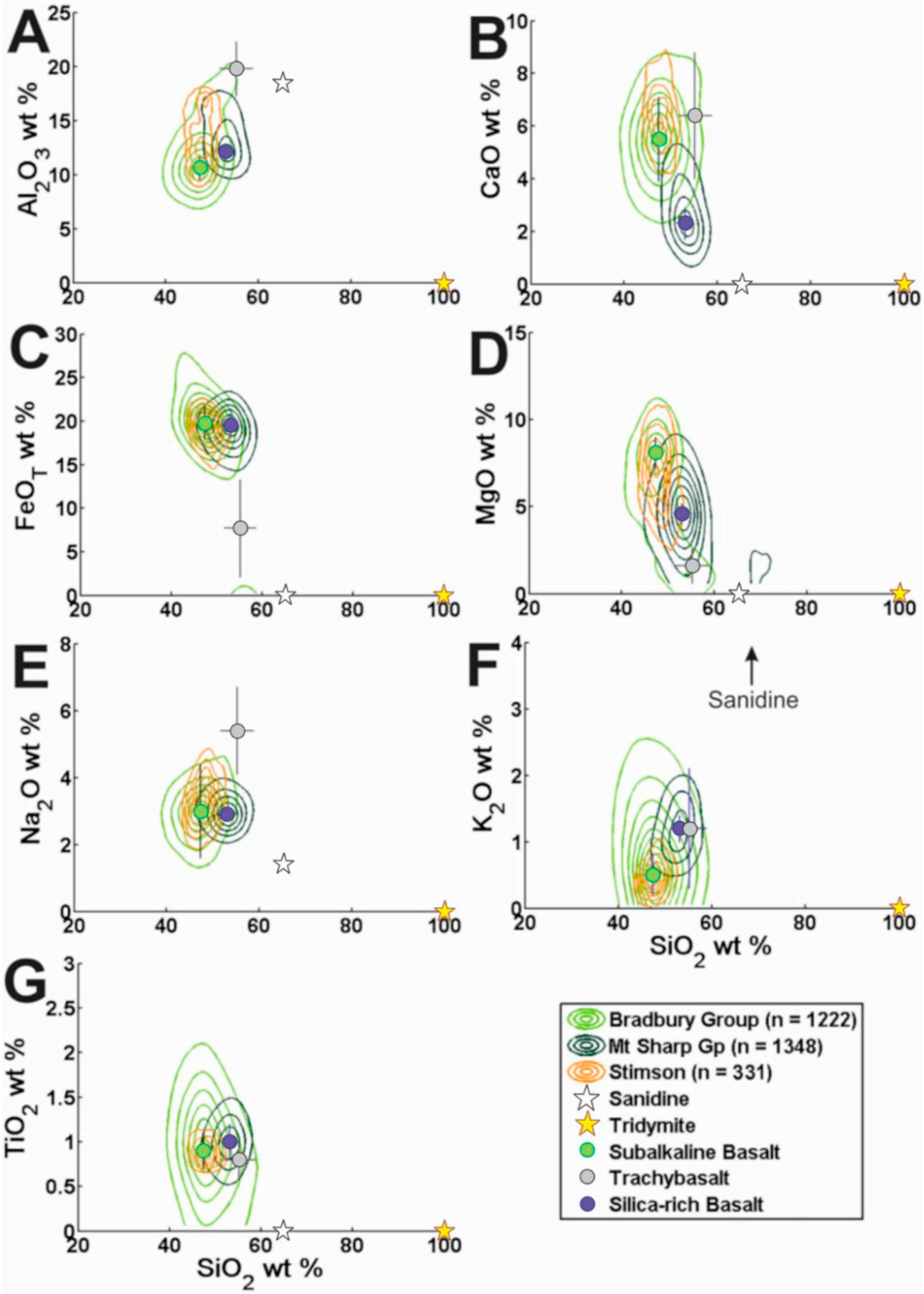

Fig. 10. Density contour Harker plots for all the stratigraphic groups in Gale crater plotted with the derived sediment endmembers calculated in Bedford et al. (2019). Bradbury and Mt. Sharp Group contours have a level step of 0.0005, bin size 100 and smoothing factor of 20. Stimson formation contours have a level step of 0.001, bin size 50 and smoothing factor 30. Sanidine and tridymite mineral compositions were taken from (Morrison et al., 2018b) and refer to the trachyte and rhyolite endmembers respectively from Treiman et al. (2016) and Morris et al. (2016).

2018). Yet, only a minor amount of olivine (up to 4.7 wt%) has been detected in the Bradbury group sandstones (Treiman et al., 2016) compared to over 9.6 wt% in the dune and soil deposits (Rampe et al., 2018). It is therefore unlikely that olivine was sourced from a Bradbury-type fluvial sandstone. Another mineralogical difference between the Stimson formation and Bradbury group is a lack of sanidine in the Stimson formation from the trachytic source that was identified at the Windjana sandstone in the Bradbury group (Treiman et al., 2016). Sediments derived from the hypothesized trachyte source region are associated with the high concentration of K_2O observed during the traverse from the Darwin outcrop to the Kimberley formation (Deit et al., 2016). The Stimson formation has a minor proportion of sanidine (2–3 wt%; Morrison et al., 2018b) that could be derived from the trachytic source. Unfortunately, this abundance, along with that of K_2O in the Stimson formation is too low to accurately define the crystalline chemistry (Morrison et al., 2018b) so we can only speculate whether it is related to a Kimberley-type sandstone. Therefore, it is most likely that the similarities in bulk geochemical composition of the Bradbury group and the Stimson formation relate to both sedimentary units being sourced from the Gale crater rim and walls with sediment recycling only contributing a minor portion of material similar to that identified in the active Bagnold dunes (Achilles et al., 2017; Rampe et al., 2018).

5. Conclusions

Mafic-felsic mineral sorting has been identified in the Stimson formation similar to the modern dunes on the surface of Mars today (Achilles et al., 2017; Cousin et al., 2017; Lapotre et al., 2017). In the Stimson formation, mineral sorting is the likely explanation for the bimodal distribution in Al_2O_3, MgO, and Na_2O for bulk Stimson (Fig. 5) and the higher bulk Al_2O_3, Na_2O and K_2O and lower bulk MgO in the Naukluft plateau compared to the Emerson plateau (Fig. 7). Clusters that likely relate to variations in mafic and felsic mineral abundances also reveal a greater proportion of felsic minerals in the Naukluft plateau than the Emerson plateau. This indicates that the net sediment transport direction and resultant wind direction of the ancient dune field was from SW–NE, opposite to that calculated for the modern aeolian Bagnold dunes (Bridges et al., 2017; Ewing et al., 2017; Lapotre et al., 2017), supporting the conclusions of Banham et al. (2018). Furthermore, the abundance of coarse, felsic minerals in the Stimson formation at the Naukluft plateau, likely presence of heavy, detrital ilmenite grains, greater compositional variation, and overall more felsic geochemistry of the Stimson formation compared to the Bagnold dunes suggests that the ancient Stimson dunes were not as well sorted in comparison to the olivine-rich, finer grained Bagnold dunes reported by Cousin et al. (2017). Hence, the Stimson formation was either derived from a more local sediment source, or the atmosphere was thicker at the time of deposition of the Stimson formation resulting in the winds that could cause the saltation of coarser grains in comparison to the dunes migrating at the surface today.

ChemCam analyses of the Stimson formation bulk geochemistry shows that it was derived from predominately basaltic material, though changes in geochemistry and mineralogy suggest input from a different basaltic source region to the modern Bagnold dunes. This difference in basaltic sediment source regions for the ancient and modern dunes is likely the result of the change in net resultant wind directions transporting the Stimson formation sediments from a source region to the SW as opposed to the Bagnold dunes that have migrated from the NE of their current locality.

The comparable bulk geochemical compositions of the Stimson formation and the Bradbury group indicate that they were derived from similar mixing of the same dominant basaltic source materials. Based on the hypothesis of previous studies that the Bradbury group basaltic sediments were likely eroded from Gale crater's Northern rim and walls (Buz et al., 2017; Deit et al., 2013; Grotzinger et al., 2015), we hypothesize that the Stimson sediments were also likely eroded and transported from the rim and walls of Gale crater situated to the SW of the Stimson formation's present location.

Declaration of competing interests

The authors declare that they have no known competing financial interests or personal relationships that could have appeared to influence the work reported in this paper.

Acknowledgements

CCB was supported through the STFC Open 2015 DTP doctoral training grant (ST/N50421X/1) to the Open University and now acknowledges support from the LPI. LPI Contribution No. 2244. LPI is operated by USRA under a cooperative agreement with the Science Mission Directorate of the National Aeronautics and Space Administration (NASA). JCB and SPS were supported through a UKSA grant (ST/P002110/1). JF acknowledges the support from the Carlsberg Foundation. The MSL engineering, ChemCam, CheMin and science teams are gratefully acknowledged for the acquisition of the data used in this paper. Support for this work in the US is provided by the NASA Mars Exploration Program and in France by CNES.

Appendix A. Supplementary data

Supplementary data to this article can be found online at https://doi.org/10.1016/j.icarus.2020.113622.

References

Achilles, C.N., Downs, R.T., Ming, D.W., Rampe, E.B., Morris, R.V., Treiman, A.H., Morrison, S.M., Blake, D.F., Vaniman, D.T., Ewing, R.C., Chipera, S.J., Yen, A.S., Bristow, T.F., Ehlmann, B.L., Gellert, R., Hazen, R.M., Fendrich, K.V., Craig, P.I., Grotzinger, J.P., Des Marais, D.J., Farmer, J.D., Sarrazin, P.C., Morookian, J.M., 2017. Mineralogy of an active eolian sediment from the Namib dune, Gale crater, Mars. J. Geophys. Res. Planets 122, 2344–2361. https://doi.org/10.1002/2017JE005262.

Anderson, R.B., Bell III, J.F., 2010. Geologic mapping and characterization of Gale crater and implications for its potential as a Mars science laboratory landing site. Mars J. 5, 76–128. doi:https://doi.org/10.1555/mars.2010.0004.

Anderson, R.B., Clegg, S.M., Frydenvang, J., Wiens, R.C., McLennan, S., Morris, R.V., Ehlmann, B., Dyar, M.D., 2017. Improved accuracy in quantitative laser-induced breakdown spectroscopy using sub-models. Spectrochim. Acta Part B At. Spectrosc. 129, 49–57. https://doi.org/10.1016/J.SAB.2016.12.002.

Bagnold, R.A., 1937. The transport of sand by wind. Geogr. J. 89, 409. https://doi.org/10.2307/1786411.

Banham, S.G., Gupta, S., Rubin, D.M., Watkins, J.A., Sumner, D.Y., Edgett, K.S., Grotzinger, J.P., Lewis, K.W., Edgar, L.A., Stack-Morgan, K.M., Barnes, R., Bell III, J. F., Day, M.D., Ewing, R.C., Lapotre, M.G.A., Stein, N.T., Rivera-Hernandez, F., Vasavada, A.R., 2018. Ancient Martian aeolian processes and palaeomorphology reconstructed from the Stimson formation on the lower slope of Aeolis Mons, Gale crater, Mars. Sedimentology 65, 993–1042. https://doi.org/10.1111/sed.12469.

Baratoux, D., Mangold, N., Arnalds, O., Bardintzeff, J.-M., Platevoët, B., Grégoire, M., Pinet, P., 2011. Volcanic sands of Iceland - diverse origins of aeolian sand deposits revealed at Dyngjusandur and Lambahraun. Earth Surf. Process. Landforms 36, 1789–1808. https://doi.org/10.1002/esp.2201.

Bedford, C.C., Bridges, J.C., Schwenzer, S.P., Wiens, R.C., Rampe, E.B., Frydenvang, J., Gasda, P.J., 2019. Alteration trends and geochemical source region characteristics preserved in the fluviolacustrine sedimentary record of Gale crater, Mars. Geochim. Cosmochim. Acta 246. https://doi.org/10.1016/j.gca.2018.11.031.

Bish, D.L., Blake, D.F., Vaniman, D.T., Chipera, S.J., Morris, R.V., Ming, D.W., Treiman, A.H., Sarrazin, P., Morrison, S.M., Downs, R.T., Achilles, C.N., Yen, A.S., Bristow, T.F., Crisp, J.A., Morookian, J.M., Farmer, J.D., Rampe, E.B., Stolper, E.M., Spanovich, N., Achilles, C., Agard, C., Verdasca, J.A.A., Anderson, R., Anderson, R., Archer, D., Armiens-Aparicio, C., Arvidson, R., Atlaskin, E., Atreya, S., Aubrey, A., Baker, B., Baker, M., Balic-Zunic, T., Baratoux, D., Baroukh, J., Barraclough, B., Bean, K., Beegle, L., Behar, A., Bell, J., Bender, S., Benna, M., Bentz, J., Berger, G., Berger, J., Berman, D., Bish, D., Blake, D.F., Avalos, J.J.B., Blaney, D., Blank, J., Blau, H., Bleacher, L., Boehm, E., Botta, O., Bottcher, S., Boucher, T., Bower, H., Boyd, N., Boynton, B., Breves, E., Bridges, J., Bridges, N., Brinckerhoff, W., Brinza, D., Bristow, T., Brunet, C., Brunner, A., Brunner, W., Buch, A., Bullock, M., Burmeister, S., Cabane, M., Calef, F., Cameron, J., Campbell, J.I., Cantor, B., Caplinger, M., Rodriguez, J.C., Carmosino, M., Blazquez, I.C., Charpentier, A., Chipera, S., Choi, D., Clark, B., Clegg, S., Cleghorn, T., Cloutis, E., Cody, G., Coll, P., Conrad, P., Coscia, D., Cousin, A., Cremers, D., Crisp, J., Cros, A., Cucinotta, F., d'Uston, C., Davis, S., Day, M.K., Juarez, M., DeFlores, L., DeLapp, D., DeMarines, J., DesMarais, D., Dietrich, W., Dingler, R., Donny, C., Downs, B., Drake, D.,

Dromart, G., Dupont, A., Duston, B., Dworkin, J., Dyar, M.D., Edgar, L., Edgett, K., Edwards, C., Edwards, L., Ehlmann, B., Ehresmann, B., Eigenbrode, J., Elliott, B., Elliott, H., Ewing, R., Fabre, C., Fairen, A., Farley, K., Farmer, J., Fassett, C., Favot, L., Fay, D., Fedosov, F., Feldman, J., Feldman, S., Fisk, M., Fitzgibbon, M., Flesch, G., Floyd, M., Fluckiger, L., Forni, O., Fraeman, A., Francis, R., Francois, P., Franz, H., Freissinet, C., French, K.L., Frydenvang, J., Gaboriaud, A., Gailhanou, M., Garvin, J., Gasnault, O., Geffroy, C., Gellert, R., Genzer, M., Glavin, D., Godber, A., Goesmann, F., Goetz, W., Golovin, D., Gomez, F.G., Gomez-Elvira, J., Gondet, B., Gordon, S., Gorevan, S., Grant, J., Griffes, J., Grinspoon, D., Grotzinger, J., Guillemot, P., Guo, J., Gupta, S., Guzewich, S., Haberle, R., Halleaux, D., Hallet, B., Hamilton, V., Hardgrove, C., Harker, D., Harpold, D., Harri, A.-M., Harshman, K., Hassler, D., Haukka, H., Hayes, A., Herkenhoff, K., Herrera, P., Hettrich, S., Heydari, E., Hipkin, V., Hoehler, T., Hollingsworth, J., Hudgins, J., Huntress, W., Hurowitz, J., Hviid, S., Iagnemma, K., Indyk, S., Israel, G., Jackson, R., Jacob, S., Jakosky, B., Jensen, E., Jensen, J.K., Johnson, J., Johnson, M., Johnstone, S., Jones, A., Jones, J., Joseph, J., Jun, I., Kah, L., Kahanpaa, H., Kahre, M., Karpushkina, N., Kasprzak, W., Kauhanen, J., Keely, L., Kemppinen, O., Keymeulen, D., Kim, M.-H., Kinch, K., King, P., Kirkland, L., Kocurek, G., Koefoed, A., Kohler, J., Kortmann, O., Kozyrev, A., Krezoski, J., Krysak, D., Kuzmin, R., Lacour, J.L., Lafaille, V., Langevin, Y., Lanza, N., Lasue, J., Le Mouelic, S., Lee, E.M., Lee, Q.-M., Lees, D., Lefavor, M., Lemmon, M., Malvitte, A.L., Leshin, L., Leveille, R., Lewin-Carpintier, E., Lewis, K., Li, S., Lipkaman, L., Little, C., Litvak, M., Lorigny, E., Lugmair, G., Lundberg, A., Lyness, E., Madsen, M., Mahaffy, P., Maki, J., Malakhov, A., Malespin, C., Malin, M., Mangold, N., Manhes, G., Manning, H., Marchand, G., Jimenez, M.M., Garcia, C.M., Martin, D., Martin, M., Martinez-Frias, J., Martin-Soler, J., Martin-Torres, F.J., Mauchien, P., Maurice, S., McAdam, A., McCartney, E., McConnochie, T., McCullough, E., McEwan, I., McKay, C., McLennan, S., McNair, S., Melikechi, N., Meslin, P.-Y., Meyer, M., Mezzacappa, A., Miller, H., Miller, K., Milliken, R., Ming, D., Minitti, M., Mischna, M., Mitrofanov, I., Moersch, J., Mokrousov, M., Jurado, A.M., Moores, J., Mora-Sotomayor, L., Morookian, J.M., Morris, R., Morrison, S., Mueller-Mellin, R., Muller, J.-P., Caro, G.M., Nachon, M., Lopez, S.N., Navarro-Gonzalez, R., Nealson, K., Nefian, A., Nelson, T., Newcombe, M., Newman, C., Newsom, H., Nikiforov, S., Niles, P., Nixon, B., Dobrea, E.N., Nolan, T., Oehler, D., Ollila, A., Olson, T., Owen, T., Hernandez, M.A., Paillet, A., Pallier, E., Palucis, M., Parker, T., Parot, Y., Patel, K., Paton, M., Paulsen, G., Pavlov, A., Pavri, B., Peinado-Gonzalez, V., Pepin, R., Peret, L., Perez, R., Perrett, G., Peterson, J., Pilorget, C., Pinet, P., Pla-Garcia, J., Plante, I., Poitrasson, F., Polkko, J., Popa, R., Posiolova, L., Posner, A., Pradler, I., Prats, B., Prokhorov, V., Purdy, S.W., Raaen, E., Radziemski, L., Rafkin, S., Ramos, M., Rampe, E., Raulin, F., Ravine, M., Reitz, G., Renno, N., Rice, M., Richardson, M., Robert, F., Robertson, K., Manfredi, J.A.R., Romeral-Planello, J.J., Rowland, S., Rubin, D., Saccoccio, M., Salamon, A., Sandoval, J., Sanin, A., Fuentes, S.A.S., Saper, L., Sarrazin, P., Sautter, V., Savijarvi, H., Schieber, J., Schmidt, M., Schmidt, W., Scholes, D.D., Schoppers, M., Schroder, S., Schwenzer, S., Martinez, E.S., Sengstacken, A., Shterts, R., Siebach, K., Siili, T., Simmonds, J., Sirven, J.-B., Slavney, S., Sletten, R., Smith, M., Sanchez, P.S., Spanovich, N., Spray, J., Squyres, S., Stack, K., Stalport, F., Steele, A., Stein, T., Stern, J., Stewart, N., Stipp, S.L.S., Stoiber, K., Stolper, E., Sucharski, B., Sullivan, R., Summons, R., Sumner, D., Sun, V., Supulver, K., Sutter, B., Szopa, C., Tan, F., Tate, C., Teinturier, S., ten Kate, I., Thomas, P., Thompson, L., Tokar, R., Toplis, M., Redondo, J.T., Trainer, M., Treiman, A., Tretyakov, V., Urqui-O'Callaghan, R., Van Beek, J., Van Beek, T., VanBommel, S., Vaniman, D., Varenikov, A., Vasavada, A., Vasconcelos, P., Vicenzi, E., Vostrukhin, A., Voytek, M., Wadhwa, M., Ward, J., Webster, C., Weigle, E., Wellington, D., Westall, F., Wiens, R.C., Wilhelm, M.B., Williams, A., Williams, J., Williams, R., Williams, R.B.M., Wilson, M., Wimmer-Schweingruber, R., Wolff, M., Wong, M., Wray, J., Wu, M., Yana, C., Yen, A., Yingst, A., Zeitlin, C., Zimdar, R., Mier, M.-P.Z., 2013. X-ray diffraction results from Mars science laboratory: mineralogy of Rocknest at Gale Crater. Science (80-.) 1238932–1238932, 341. https://doi.org/10.1126/science.1238932.

Bish, D., Blake, D., Vaniman, D., Sarrazin, P., Bristow, T., Achilles, C., Dera, P., Chipera, S., Crisp, J., Downs, R.T., Farmer, J., Gailhanou, M., Ming, D., Morookian, J.M., Morris, R., Morrison, S., Rampe, E., Treiman, A., Yen, A., 2014. The first X-ray diffraction measurements on Mars. IUCrJ 1, 514–522. https://doi.org/10.1107/S2052252514021150.

Blake, D., Vaniman, D., Achilles, C., Anderson, R., Bish, D., Bristow, T., Chen, C., Chipera, S., Crisp, J., Des Marais, D., Downs, R.T., Farmer, J., Feldman, S., Fonda, M., Gailhanou, M., Ma, H., Ming, D.W., Morris, R.V., Sarrazin, P., Stolper, E., Treiman, A., Yen, A., 2012. Characterization and calibration of the CheMin mineralogical instrument on Mars Science Laboratory. Space Sci. Rev. 170, 341–399. https://doi.org/10.1007/s11214-012-9905-1.

Blaney, D.L., Wiens, R.C., Maurice, S., Clegg, S.M., Anderson, R.B., Kah, L.C., Le Mouélic, S., Ollila, A., Bridges, N., Tokar, R., Berger, G., Bridges, J.C., Cousin, A., Clark, B., Dyar, M.D., King, P.L., Lanza, N., Mangold, N., Meslin, P.-Y., Newsom, H., Schröder, S., Rowland, S., Johnson, J., Edgar, L., Gasnault, O., Forni, O., Schmidt, M., Goetz, W., Stack, K., Sumner, D., Fisk, M., Madsen, M.B., 2014. Chemistry and texture of the rocks at Rocknest, Gale Crater: evidence for sedimentary origin and diagenetic alteration. J. Geophys. Res. Planets 119, 2109–2131. https://doi.org/10.1002/2013JE004590.

Bridges, N.T., Ehlmann, B.L., 2018. The Mars Science Laboratory (MSL) Bagnold Dunes Campaign, Phase I: overview and introduction to the special issue. J. Geophys. Res. Planets 123, 3–19. https://doi.org/10.1002/2017JE005401.

Bridges, J.C., Schwenzer, S.P., Leveille, R., Westall, F., Wiens, R.C., Mangold, N., Bristow, T., Edwards, P., Berger, G., 2015. Diagenesis and clay mineral formation at Gale Crater, Mars. J. Geophys. Res. Planets 120, 1–19. https://doi.org/10.1002/2014JE004757.

Bridges, N.T., Sullivan, R., Newman, C.E., Navarro, S., van Beek, J., Ewing, R.C., Ayoub, F., Silvestro, S., Gasnault, O., Le Mouélic, S., Lapotre, M.G.A., Rapin, W., 2017. Martian aeolian activity at the Bagnold Dunes, Gale Crater: the view from the surface and orbit. J. Geophys. Res. Planets 122, 2077–2110. https://doi.org/10.1002/2017JE005263.

Bristow, T.F., Rampe, E.B., Achilles, C.N., Blake, D.F., Chipera, S.J., Craig, P., Crisp, J.A., Des Marais, D.J., Downs, R.T., Gellert, R., Grotzinger, J.P., Gupta, S., Hazen, R.M., Horgan, B., Hogancamp, J.V., Mangold, N., Mahaffy, P.R., McAdam, A.C., Ming, D. W., Morookian, J.M., Morris, R.V., Morrison, S.M., Treiman, A.H., Vaniman, D.T., Vasavada, A.R., Yen, A.S., 2018. Clay mineral diversity and abundance in sedimentary rocks of Gale crater, Mars. Sci. Adv. 4, eaar3330 https://doi.org/10.1126/sciadv.aar3330.

Bryk, A.B., Dietrich, W.E., Lamb, M.P., Grotzinger, J.P., Vasavada, A.R., Stack, K.M., Arvidson, R., Fedo, C., Bennett, K., Fox, V.K., Gupta, S., Wiens, R.C., Williams, R.M. E., 2019. In curiosity's path: the geomorphology and stratigraphy of the Greenheugh Pediment and Gediz Vallis Ridge in Gale Crater. In: 50th Lunar Planet. Sci. Conf. Held 18–22 March, 2019 Woodlands, Texas. LPI Contrib. No. 2132, Id.2263 50.

Buz, J., Ehlmann, B.L., Pan, L., Grotzinger, J.P., 2017. Mineralogy and stratigraphy of the Gale crater rim, wall, and floor units. J. Geophys. Res. Planets 122, 1090–1118. https://doi.org/10.1002/2016JE005163.

Cardenas, B.T., Kocurek, G., Mohrig, D., Swanson, T., Hughes, C.M., Brothers, S.C., 2019. Preservation of autogenic processes and allogenic forcings in set-scale Aeolian architecture II: the scour-and-fill dominated Jurassic Page Sandstone, Arizona, U.S. A. J. Sediment. Res. 89, 741–760. https://doi.org/10.2110/jsr.2019.41.

Carr, M., 2007. The Surface of Mars, 6th ed. Cambridge University Press.

Chan, M., Potter, S., Peterson, E., Parry, W., Bowman, J., Grotzinger, J., Milliken, R., 2012. Characteristics of terrestrial ferric oxide concretions and implications for Mars. Sediment. Geol. Mars 102, 253–270.

Clegg, S.M., Wiens, R.C., Anderson, R., Forni, O., Frydenvang, J., Lasue, J., Cousin, A., Payré, V., Boucher, T., Dyar, M.D., McLennan, S.M., Morris, R.V., Graff, T.G., Mertzman, S.A., Ehlmann, B.L., Belgacem, I., Newsom, H., Clark, B.C., Melikechi, N., Mezzacappa, A., McInroy, R.E., Martinez, R., Gasda, P., Gasnault, O., Maurice, S., 2017. Recalibration of the Mars Science Laboratory ChemCam instrument with an expanded geochemical database. Spectrochim. Acta Part B At. Spectrosc. 129, 64–85. https://doi.org/10.1016/J.SAB.2016.12.003.

Cousin, A., Meslin, P.Y., Wiens, R.C., Rapin, W., Mangold, N., Fabre, C., Gasnault, O., Forni, O., Tokar, R., Ollila, A., Schröder, S., Lasue, J., Maurice, S., Sautter, V., Newsom, H., Vaniman, D., Le Mouélic, S., Dyar, D., Berger, G., Blaney, D., Nachon, M., Dromart, G., Lanza, N., Clark, B., Clegg, S., Goetz, W., Berger, J., Barraclough, B., Delapp, D., 2015. Compositions of coarse and fine particles in Martian soils at gale: a window into the production of soils. Icarus 249, 22–42. https://doi.org/10.1016/J.ICARUS.2014.04.052.

Cousin, A., Dehouck, E., Meslin, P.Y., Forni, O., Williams, A.J., Stein, N., Gasnault, O., Bridges, N., Ehlmann, B., Schröder, S., Payré, V., Rapin, W., Pinet, P., Sautter, V., Lanza, N., Lasue, J., Maurice, S., Wiens, R.C., 2017. Geochemistry of the Bagnold dune field as observed by ChemCam and comparison with other aeolian deposits at Gale Crater. J. Geophys. Res. Planets 122, 2144–2162. https://doi.org/10.1002/2017JE005261.

Craddock, R.A., 2012. Aeolian processes on the terrestrial planets. Prog. Phys. Geogr. Earth Environ. 36, 110–124. https://doi.org/10.1177/0309133311425399.

Czarnecki, S., Hardgrove, C., Gasda, P.J., Rapin, W., Frydenvang, J., Gabriel, T.S.J., Litvak, M.L., Nowicki, S., Wiens, R.C., Thompson, L.M., Newsom, H.E., Calef, F.J.. I., Gengl, H., 2018. Characterizing the subsurface distribution of high-silica features at Gale crater, Mars using active neutron experiments and LIBS geochemistry. Am. Geophys. Union, Fall Meet. 2018, (Abstr. #P31F-3758).

Day, M., Anderson, W., Kocurek, G., Mohrig, D., 2016. Carving intracrater layered deposits with wind on Mars. Geophys. Res. Lett. 43, 2473–2479. https://doi.org/10.1002/2016GL068011@10.1002/(ISSN)1944-8007.2016GRLEDHIGH.

Deit, L.L., Hauber, E., Fueten, F., Pondrelli, M., Rossi, A.P., Jaumann, R., 2013. Sequence of infilling events in Gale Crater, Mars: results from morphology, stratigraphy, and mineralogy. J. Geophys. Res. Planets 118, 2439–2473. https://doi.org/10.1002/2012JE004322.

Deit, L.L., Mangold, N., Forni, O., Cousin, A., Lasue, J., Schröder, S., Wiens, R.C., Sumner, D., Fabre, C., Stack, K.M., Anderson, R.B., Blaney, D., Clegg, S., Dromart, G., Fisk, M., Gasnault, O., Grotzinger, J.P., Gupta, S., Lanza, N., Mouélic, S.L., Maurice, S., McLennan, S.M., Meslin, P.-Y., Nachon, M., Newsom, H., Payré, V., Rapin, W., Rice, M., Sautter, V., Treiman, A.H., 2016. The potassic sedimentary rocks in Gale Crater, Mars, as seen by ChemCam on board Curiosity. J. Geophys. Res. Planets 121, 784–804. https://doi.org/10.1002/2015JE004987@10.1002/(ISSN)2169-9100.MSLRM1.

Dott Jr., R.H., 2003. The importance of Eolian abrasion in Supermature quartz sandstones and the paradox of weathering on vegetation free landscapes. J. Geol. 111, 387–405. https://doi.org/10.1086/375286.

Edgar, L., Fedo, C., Gupta, S., Banham, S., Fraeman, A., Grotzinger, J., Stack Morgan, K., Stein, N., Bennet, K., Rivera-Hernández, F., Sun, V., Edgett, K., Rubin, D., House, C., Van Beek, J., 2020. A lacustrine paleoenvironment recorded at Vera Rubin Ridge, Gale crater: Overview of the sedimentology and stratigraphy observed by the Mars Science Laboratory Curiosity rover. Earth and Space Science Open Archive. https://doi.org/10.1002/essoar.10501350.1.

Edgett, K.S., Yingst, R.A., Ravine, M.A., Caplinger, M.A., Maki, J.N., Ghaemi, F.T., Schaffner, J.A., Bell, J.F., Edwards, L.J., Herkenhoff, K.E., Heydari, E., Kah, L.C., Lemmon, M.T., Minitti, M.E., Olson, T.S., Parker, T.J., Rowland, S.K., Schieber, J., Sullivan, R.J., Sumner, D.Y., Thomas, P.C., Jensen, E.H., Simmonds, J.J., Sengstacken, A.J., Willson, R.G., Goetz, W., 2012. Curiosity's Mars Hand Lens Imager (MAHLI) investigation. Space Sci. Rev. 170, 259–317. https://doi.org/10.1007/s11214-012-9910-4.

Edwards, P.H., Bridges, J.C., Wiens, R., Anderson, R., Dyar, D., Fisk, M., Thompson, L., Gasda, P., Filiberto, J., Schwenzer, S.P., Blaney, D., Hutchinson, I., 2017. Basalt-trachybasalt samples in Gale Crater, Mars. Meteorit. Planet. Sci. 52, 2410–2931. https://doi.org/10.1111/maps.12953.

Ehlmann, B.L., Buz, J., 2015. Mineralogy and fluvial history of the watersheds of Gale, Knobel, and Sharp craters: a regional context for the Mars Science Laboratory Curiosity's exploration. Geophys. Res. Lett. 42, 264–273. https://doi.org/10.1002/2014GL062553.

Ehlmann, B.L., Edgett, K.S., Sutter, B., Achilles, C.N., Litvak, M.L., Lapotre, M.G.A., Sullivan, R., Fraeman, A.A., Arvidson, R.E., Blake, D.F., Bridges, N.T., Conrad, P.G., Cousin, A., Downs, R.T., Gabriel, T.S.J., Gellert, R., Hamilton, V.E., Hardgrove, C., Johnson, J.R., Kuhn, S., Mahaffy, P.R., Maurice, S., McHenry, M., Meslin, P.-Y., Ming, D.W., Minitti, M.E., Morookian, J.M., Morris, R.V., O'Connell-Cooper, C.D., Pinet, P.C., Rowland, S.K., Schröder, S., Siebach, K.L., Stein, N.T., Thompson, L.M., Vaniman, D.T., Vasavada, A.R., Wellington, D.F., Wiens, R.C., Yen, A.S., 2017. Chemistry, mineralogy, and grain properties at Namib and High dunes, Bagnold dune field, Gale crater, Mars: a synthesis of Curiosity rover observations. J. Geophys. Res. Planets 122, 2510–2543. https://doi.org/10.1002/2017JE005267.

Eilers, P.H.C., Goeman, J.J., 2004. Enhancing scatterplots with smoothed densities. Bioinformatics 20, 623–628. https://doi.org/10.1093/bioinformatics/btg454.

Ewing, R.C., Kocurek, G., 2010. Aeolian dune-field pattern boundary conditions. Geomorphology 114, 175–187. https://doi.org/10.1016/J.GEOMORPH.2009.06.015.

Ewing, R.C., Lapotre, M.G.A., Lewis, K.W., Day, M., Stein, N., Rubin, D.M., Sullivan, R., Banham, S., Lamb, M.P., Bridges, N.T., Gupta, S., Fischer, W.W., 2017. Sedimentary processes of the Bagnold Dunes: implications for the eolian rock record of Mars. J. Geophys. Res. Planets 122, 2544–2573. https://doi.org/10.1002/2017JE005324.

Fedo, C.M., Grotzinger, J.P., Gupta, S., Fraeman, A., Edgar, L., Edgett, K., Stein, N., Rivera-Hernandez, F., Lewis, K., Stack, K.M., House, C., Rubin, D., Vasavada, A.R., 2018. Sedimentology and stratigraphy of the Murray Formation, Gale Crater, Mars. In: 49th Lunar Planet. Sci. Conf. 19–23 March, 2018, Held Woodlands, Texas LPI Contrib. No. 2083, Id.2078 49.

Forni, O., Maurice, S., Gasnault, O., Wiens, R.C., Cousin, A., Clegg, S.M., Sirven, J.-B., Lasue, J., 2013. Independent component analysis classification of laser induced breakdown spectroscopy spectra. Spectrochim. Acta Part B At. Spectrosc. 86, 31–41. https://doi.org/10.1016/j.sab.2013.05.003.

Fraeman, A.A., Arvidson, R.E., Catalano, J.G., Grotzinger, J.P., Morris, R.V., Murchie, S. L., Stack, K.M., Humm, D.C., McGovern, J.A., Seelos, F.P., Seelos, K.D., Viviano, C.E., 2013. A hematite-bearing layer in Gale Crater, Mars: mapping and implications for past aqueous conditions. Geology 41, 1103–1106. https://doi.org/10.1130/G34613.1.

Fraeman, A.A., Ehlmann, B.L., Arvidson, R.E., Edwards, C.S., Grotzinger, J.P., Milliken, R.E., Quinn, D.P., Rice, M.S., 2016. The stratigraphy and evolution of lower Mount Sharp from spectral, morphological, and thermophysical orbital data sets. J. Geophys. Res. Planets 121, 1713–1736. https://doi.org/10.1002/2016JE005095.

Frydenvang, J., Gasda, P.J., Hurowitz, J.A., Grotzinger, J.P., Wiens, R.C., Newsom, H.E., Edgett, K.S., Watkins, J., Bridges, J.C., Maurice, S., Fisk, M.R., Johnson, J.R., Rapin, W., Stein, N.T., Clegg, S.M., Schwenzer, S.P., Bedford, C.C., Edwards, P., Mangold, N., Cousin, A., Anderson, R.B., Payré, V., Vaniman, D., Blake, D.F., Lanza, N.L., Gupta, S., Van Beek, J., Sautter, V., Meslin, P.-Y., Rice, M., Milliken, R., Gellert, R., Thompson, L., Clark, B.C., Sumner, D.Y., Fraeman, A.A., Kinch, K.M., Madsen, M.B., Mitrofanov, I.G., Jun, I., Calef, F., Vasavada, A.R., 2017. Diagenetic silica enrichment and late-stage groundwater activity in Gale crater, Mars. Geophys. Res. Lett. 44, 4716–4724. https://doi.org/10.1002/2017GL073323.

Gabriel, T.S.J., Hardgrove, C., Czarnecki, S., Rampe, E.B., Rapin, W., Achilles, C.N., Sullivan, D., Nowicki, S., Thompson, L., Litvak, M., Mitrofanov, I., Downs, R.T., 2018. Water abundance of dunes in Gale Crater, Mars from active neutron experiments and implications for amorphous phases. Geophys. Res. Lett. 45, 12,766–12,775. https://doi.org/10.1029/2018GL079045.

Garzanti, E., Vermeesch, P., Andò, S., Vezzoli, G., Valagussa, M., Allen, K., Kadi, K.A., Al-Juboury, A.I.A., 2013. Provenance and recycling of Arabian desert sand. Earth-Science Rev 120, 1–19. https://doi.org/10.1016/J.EARSCIREV.2013.01.005.

Gasnault, O., Forni, O., Meslin, P.-Y., Maurice, S., Wiens, R.C., Anderson, R.B., Berger, G., Clegg, S.M., Cousin, A., d'Uston, C., Lasue, J., Lewin, E., Melikechi, N., Newsom, H. E., Pinet, P., Team, M.S., 2013. ChemCam target classification: who's who from Curiosity's first ninety sols. 44th Lunar Planet. Sci. Conf. Held March 18–22, 2013 Woodlands, Texas. LPI Contrib. No. 1719, p.1994 44, 1994.

Gasnault, O., Pinet, P., Wiens, R.C., Dehouck, E., Gasda, P., Forni, O., Lasue, J., Stack, K., Maurice, S., Fabre, C., 2019. Targeting and Classifying Drill Holes on Mars with ChemCam (LPI Contrib. 2089).

Gellert, R., Clark, B.C., 2015. In situ compositional measurements of rocks and soils with the alpha particle X-ray spectrometer on NASA's Mars rovers. Elements 11, 39–44. https://doi.org/10.2113/gselements.11.1.39.

Grotzinger, J.P., Crisp, J., Vasavada, A.R., Anderson, R.C., Baker, C.J., Barry, R., Blake, D.F., Conrad, P., Edgett, K.S., Ferdowski, B., Gellert, R., Gilbert, J.B., Golombek, M., Gómez-Elvira, J., Hassler, D.M., Jandura, L., Litvak, M., Mahaffy, P., Maki, J., Meyer, M., Malin, M.C., Mitrofanov, I., Simmonds, J.J., Vaniman, D., Welch, R.V., Wiens, R.C., 2012. Mars science laboratory mission and science investigation. Space Sci. Rev. 170, 5–56. https://doi.org/10.1007/s11214-012-9892-2.

Grotzinger, J.P., Sumner, D.Y., Kah, L.C., Stack, K., Gupta, S., Edgar, L., Rubin, D., Lewis, K., Schieber, J., Mangold, N., Milliken, R., Conrad, P.G., DesMarais, D., Farmer, J., Siebach, K., Calef, F., Hurowitz, J., McLennan, S.M., Ming, D., Vaniman, D., Crisp, J., Vasavada, A., Edgett, K.S., Malin, M., Blake, D., Gellert, R., Mahaffy, P., Wiens, R.C., Maurice, S., Grant, J.A., Wilson, S., Anderson, R.C., Beegle, L., Arvidson, R., Hallet, B., Sletten, R.S., Rice, M., Bell, J., Griffes, J., Ehlmann, B., Anderson, R.B., Bristow, T.F., Dietrich, W.E., Dromart, G., Eigenbrode, J., Fraeman, A., Hardgrove, C., Herkenhoff, K., Jandura, L., Kocurek, G., Lee, S., Leshin, L.A., Leveille, R., Limonadi, D., Maki, J., McCloskey, S., Meyer, M., Minitti, M., Newsom, H., Oehler, D., Okon, A., Palucis, M., Parker, T., Rowland, S., Schmidt, M., Squyres, S., Steele, A., Stolper, E., Summons, R., Treiman, A., Williams, R., Yingst, A., 2014. A habitable fluvio-lacustrine environment at Yellowknife Bay, Gale crater, Mars. Science (80-.) 343, 1242777. https://doi.org/10.1126/science.1242777.

Grotzinger, J.P., Gupta, S., Malin, M.C., Rubin, D.M., Schieber, J., Siebach, K., Sumner, D.Y., Stack, K.M., Vasavada, A.R., Arvidson, R.E., Calef, F., Edgar, L., Fischer, W.F., Grant, J.A., Griffes, J., Kah, L.C., Lamb, M.P., Lewis, K.W., Mangold, N., Minitti, M.E., Palucis, M., Rice, M., Williams, R.M.E., Yingst, R.A., Blake, D., Blaney, D., Conrad, P., Crisp, J., Dietrich, W.E., Dromart, G., Edgett, K.S., Ewing, R.C., Gellert, R., Hurowitz, J.A., Kocurek, G., Mahaffy, P., McBride, M.J., McLennan, S.M., Mischna, M., Ming, D., Milliken, R., Newsom, H., Oehler, D., Parker, T.J., Vaniman, D., Wiens, R.C., Wilson, S.A., 2015. Deposition, exhumation, and paleoclimate of an ancient lake deposit, Gale crater, Mars. Science (80-.) 350, aac7575–aac7575. https://doi.org/10.1126/science.aac7575.

Hausrath, E.M., Ming, D.W., Peretyazhko, T.S., Rampe, E.B., 2018. Reactive transport and mass balance modeling of the Stimson sedimentary formation and altered fracture zones constrain diagenetic conditions at Gale crater. Mars. Earth Planet. Sci. Lett. 491, 1–10. https://doi.org/10.1016/J.EPSL.2018.02.037.

Hobbs, S.W., Paull, D.J., Bourke, M.C., 2010. Aeolian processes and dune morphology in Gale Crater. Icarus 210, 102–115. https://doi.org/10.1016/J.ICARUS.2010.06.006.

Hurowitz, J.A., Grotzinger, J.P., Fischer, W.W., McLennan, S.M., Milliken, R.E., Stein, N., Vasavada, A.R., Blake, D.F., Dehouck, E., Eigenbrode, J.L., Fairén, A.G., Frydenvang, J., Gellert, R., Grant, J.A., Gupta, S., Herkenhoff, K.E., Ming, D.W., Rampe, E.B., Schmidt, M.E., Siebach, K.L., Stack-Morgan, K., Sumner, D.Y., Wiens, R. C., 2017. Redox stratification of an ancient lake in Gale Crater, Mars. Science 356. https://doi.org/10.1126/science.aah6849.

Irvine, T.N., Baragar, W.R.A., 1971. A Guide to the Chemical Classification of the Common Volcanic Rocks. Canadian Journal of Earth Sciences 8, 523–548. https://doi.org/10.1139/e71-055.

Johnson, J.R., Achilles, C., Bell, J.F., Bender, S., Cloutis, E., Ehlmann, B., Fraeman, A., Gasnault, O., Hamilton, V.E., Le Mouélic, S., Maurice, S., Pinet, P., Thompson, L., Wellington, D., Wiens, R.C., 2017. Visible/near-infrared spectral diversity from in situ observations of the Bagnold Dune Field sands in Gale Crater, Mars. J. Geophys. Res. Planets 122, 2655–2684. https://doi.org/10.1002/2016JE005187.

Kite, E.S., Lewis, K.W., Lamb, M.P., Newman, C.E., Richardson, M.I., 2013. Growth and form of the mound in Gale Crater, Mars: slope wind enhanced erosion and transport. Geology 41, 543–546. https://doi.org/10.1130/G33909.1.

Kocurek, G., 1988. First-order and super bounding surfaces in eolian sequences—bounding surfaces revisited. Sediment. Geol. 56, 193–206.

Kocurek, G., 1991. Interpretation of ancient Eolian Sand Dunes. Annu. Rev. Earth Planet. Sci. 19, 43–75. https://doi.org/10.1146/annurev.ea.19.050191.000355.

Kok, J.F., Parteli, E.J.R., Michaels, T.I., Karam, D.B., 2012. The physics of wind-blown sand and dust. Reports Prog. Phys. 75, 106901 https://doi.org/10.1088/0034-4885/75/10/106901.

Kronyak, R.E., Kah, L.C., Miklusicak, N.B., Edgett, K.S., Sun, V.Z., Bryk, A.B., Williams, R. M.E., 2019. Extensive polygonal fracture network in Siccar point group strata: fracture mechanisms and implications for fluid circulation in Gale Crater, Mars. J. Geophys. Res. Planets 0. https://doi.org/10.1029/2019JE006125.

Lapotre, M.G.A., Rampe, E.B., 2018. Curiosity's investigation of the Bagnold Dunes, Gale Crater: overview of the two-phase scientific campaign and introduction to the special collection. Geophys. Res. Lett. 45, 10,200–10,210. https://doi.org/10.1029/2018GL079032.

Lapotre, M.G.A., Ehlmann, B.L., Minson, S.E., Arvidson, R.E., Ayoub, F., Fraeman, A.A., Ewing, R.C., Bridges, N.T., 2017. Compositional variations in sands of the Bagnold Dunes, Gale crater, Mars, from visible-shortwave infrared spectroscopy and comparison with ground truth from the Curiosity rover. J. Geophys. Res. Planets 122, 2489–2509. https://doi.org/10.1002/2016JE005133.

Lasue, J., Cousin, A., Meslin, P.-Y., Mangold, N., Wiens, R.C., Berger, G., Dehouck, E., Forni, O., Goetz, W., Gasnault, O., Rapin, W., Schroeder, S., Ollila, A., Johnson, J., Le Mouélic, S., Maurice, S., Anderson, R., Blaney, D., Clark, B., Clegg, S.M., d'Uston, C., Fabre, C., Lanza, N., Madsen, M.B., Martin-Torres, J., Melikechi, N., Newsom, H., Sautter, V., Zorzano, M.P., 2018. Martian Eolian dust probed by ChemCam. Geophys. Res. Lett. 45, 10,968–10,977. https://doi.org/10.1029/2018GL079210.

Le Mouélic, S., Gasnault, O., Herkenhoff, K.E., Bridges, N.T., Langevin, Y., Mangold, N., Maurice, S., Wiens, R.C., Pinet, P., Newsom, H.E., Deen, R.G., Bell, J.F., Johnson, J. R., Rapin, W., Barraclough, B., Blaney, D.L., Deflores, L., Maki, J., Malin, M.C., Pérez, R., Saccoccio, M., 2015. The ChemCam remote micro-imager at Gale crater: review of the first year of operations on Mars. Icarus 249, 93–107. https://doi.org/10.1016/J.ICARUS.2014.05.030.

Léveillé, R.J., Bridges, J., Wiens, R.C., Mangold, N., Cousin, A., Lanza, N., Forni, O., Ollila, A., Grotzinger, J., Clegg, S., Siebach, K., Berger, G., Clark, B., Fabre, C., Anderson, R., Gasnault, O., Blaney, D., Deflores, L., Leshin, L., Maurice, S., Newsom, H., 2014. Chemistry of fracture-filling raised ridges in Yellowknife Bay, Gale Crater: window into past aqueous activity and habitability on Mars. J. Geophys. Res. Planets 119, 2398–2415. https://doi.org/10.1002/2014JE004620.

Malin, M.C., Edgett, K.S., Dietrich, W.E., Gupta, S., Sumner, D.Y., Wiens, R.C., Mangold, N., Malin, M.C., Edgett, K.S., Maurice, S., Forni, O., Gasnault, O., Ollila, A., Newsom, H.E., Dromart, G., Palucis, M.C., Yingst, R.A., Anderson, R.B., Herkenhoff, K.E., Mouélic, S.L., Goetz, W., Madsen, M.B., Koefoed, A., Jensen, J.K., Bridges, J.C., Schwenzer, S.P., Lewis, K.W., Stack, K.M., Rubin, D., Kah, L.C., Bell, J. F., Farmer, J.D., Sullivan, R., Beek, T.V., Blaney, D.L., Pariser, O., Deen, R.G.,

Team, M.S., 2000. Sedimentary rocks of early Mars. Science (80-.) 290, 1927–1937. https://doi.org/10.1126/science.290.5498.1927.

Malin, M.C., Ravine, M.A., Caplinger, M.A., Tony Ghaemi, F., Schaffner, J.A., Maki, J.N., Bell, J.F., Cameron, J.F., Dietrich, W.E., Edgett, K.S., Edwards, L.J., Garvin, J.B., Hallet, B., Herkenhoff, K.E., Heydari, E., Kah, L.C., Lemmon, M.T., Minitti, M.E., Olson, T.S., Parker, T.J., Rowland, S.K., Schieber, J., Sletten, R., Sullivan, R.J., Sumner, D.Y., Aileen Yingst, R., Duston, B.M., McNair, S., Jensen, E.H., 2017. The Mars science laboratory (MSL) mast cameras and descent imager: investigation and instrument descriptions. Earth Sp. Sci. 4, 506–539. https://doi.org/10.1002/2016EA000252.

Mangold, N., Baratoux, D., Arnalds, O., Bardintzeff, J.-M., Platevoet, B., Grégoire, M., Pinet, P., 2011. Segregation of olivine grains in volcanic sands in Iceland and implications for Mars. Earth Planet. Sci. Lett. 310, 233–243. https://doi.org/10.1016/J.EPSL.2011.07.025.

Mangold, N., Thompson, L.M., Forni, O., Williams, A.J., Fabre, C., Le Deit, L., Wiens, R. C., Williams, R., Anderson, R.B., Blaney, D.L., Calef, F., Cousin, A., Clegg, S.M., Dromart, G., Dietrich, W.E., Edgett, K.S., Fisk, M.R., Gasnault, O., Gellert, R., Grotzinger, J.P., Kah, L., Le Mouélic, S., McLennan, S.M., Maurice, S., Meslin, P.-Y., Newsom, H.E., Palucis, M.C., Rapin, W., Sautter, V., Siebach, K.L., Stack, K., Sumner, D., Yingst, A., 2016. Composition of conglomerates analyzed by the curiosity rover: implications for Gale Crater crust and sediment sources. J. Geophys. Res. Planets 121, 353–387. https://doi.org/10.1002/2015JE004977.

Mangold, N., Schmidt, M.E., Fisk, M.R., Forni, O., McLennan, S.M., Ming, D.W., Sautter, V., Sumner, D., Williams, A.J., Clegg, S.M., Cousin, A., Gasnault, O., Gellert, R., Grotzinger, J.P., Wiens, R.C., 2017. Classification scheme for sedimentary and igneous rocks in Gale crater, Mars. Icarus 284, 1–17. https://doi.org/10.1016/J.ICARUS.2016.11.005.

Maurice, S., Wiens, R.C., Saccoccio, M., Barraclough, B., Gasnault, O., Forni, O., Mangold, N., Baratoux, D., Bender, S., Berger, G., Bernardin, J., Berthé, M., Bridges, N., Blaney, D., Bouyé, M., Caïs, P., Clark, B., Clegg, S., Cousin, A., Cremers, D., Cros, A., Deflores, L., Derycke, C., Dingler, B., Dromart, G., Dubois, B., Dupieux, M., Durand, E., D'Uston, L., Fabre, C., Faure, B., Gaboriaud, A., Gharsa, T., Herkenhoff, K., Kan, E., Kirkland, L., Kouach, D., Lacour, J.L., Langevin, Y., Lasue, J., Le Mouélic, S., Lescure, M., Lewin, E., Limonadi, D., Manhès, G., Mauchien, P., McKay, C., Meslin, P.Y., Michel, Y., Miller, E., Newsom, H.E., Orttner, G., Paillet, A., Parès, L., Parot, Y., Pérez, R., Pinet, P., Poitrasson, F., Quertier, B., Sallé, B., Sotin, C., Sautter, V., Séran, H., Simmonds, J.J., Sirven, J.B., Stiglich, R., Striebig, N., Thocaven, J.J., Toplis, M.J., Vaniman, D., 2012. The ChemCam instrument suite on the Mars Science Laboratory (MSL) rover: science objectives and mast unit description. Space Sci. Rev. 170, 95–166. https://doi.org/10.1007/s11214-012-9912-2.

Maurice, S., Clegg, S.M., Wiens, R.C., Gasnault, O., Rapin, W., Forni, O., Cousin, A., Sautter, V., Mangold, N., Le Deit, L., Nachon, M., Anderson, R.B., Lanza, N.L., Fabre, C., Payré, V., Lasue, J., Meslin, P.-Y., Léveillé, R.J., Barraclough, B.L., Beck, P., Bender, S.C., Berger, G., Bridges, J.C., Bridges, N.T., Dromart, G., Dyar, M. D., Francis, R., Frydenvang, J., Gondet, B., Ehlmann, B.L., Herkenhoff, K.E., Johnson, J.R., Langevin, Y., Madsen, M.B., Melikechi, N., Lacour, J.-L., Le Mouélic, S., Lewin, E., Newsom, H.E., Ollila, A.M., Pinet, P., Schröder, S., Sirven, J.-B., Tokar, R.L., Toplis, M.J., d'Uston, C., Vaniman, D.T., Vasavada, A.R., 2016. ChemCam activities and discoveries during the nominal mission of the Mars Science Laboratory in Gale crater, Mars. J. Anal. At. Spectrom. 31, 863–889. https://doi.org/10.1039/C5JA00417A.

McLennan, S.M., Anderson, R.B., Bell, J.F., Bridges, J.C., Calef, F., Campbell, J.L., Clark, B.C., Clegg, S., Conrad, P., Cousin, A., Des Marais, D.J., Dromart, G., Dyar, M. D., Edgar, L.A., Ehlmann, B.L., Fabre, C., Forni, O., Gasnault, O., Gellert, R., Gordon, S., Grant, J.A., Grotzinger, J.P., Gupta, S., Herkenhoff, K.E., Hurowitz, J.A., King, P.L., Le Mouélic, S., Leshin, L.A., Léveillé, R., Lewis, K.W., Mangold, N., Maurice, S., Ming, D.W., Morris, R.V., Nachon, M., Newsom, H.E., Ollila, A.M., Perrett, G.M., Rice, M.S., Schmidt, M.E., Schwenzer, S.P., Stack, K., Stolper, E.M., Sumner, D.Y., Treiman, A.H., VanBommel, S., Vaniman, D.T., Vasavada, A., Wiens, R.C., Yingst, R.A., MSL Science Team, M.S, 2014. Elemental geochemistry of sedimentary rocks at Yellowknife Bay, Gale crater, Mars. Science 343, 1244734. https://doi.org/10.1126/science.1244734.

McSween, H.Y., Ruff, S.W., Morris, R.V., Bell, J.F., Herkenhoff, K., Gellert, R., Stockstill, K.R., Tornabene, L.L., Squyres, S.W., Crisp, J.A., Christensen, P.R., McCoy, T.J., Mittlefehldt, D.W., Schmidt, M., 2006. Alkaline volcanic rocks from the Columbia Hills, Gusev crater, Mars. J. Geophys. Res. 111, E09S91 https://doi.org/10.1029/2006JE002698.

Meslin, P.-Y., Gasnault, O., Forni, O., Schröder, S., Cousin, A., Berger, G., Clegg, S.M., Lasue, J., Maurice, S., Sautter, V., Le Mouélic, S., Wiens, R.C., Fabre, C., Goetz, W., Bish, D., Mangold, N., Ehlmann, B., Lanza, N., Harri, A.-M., Anderson, R., Rampe, E., McConnochie, T.H., Pinet, P., Blaney, D., Léveillé, R., Archer, D., Barraclough, B., Bender, S., Blake, D., Blank, J.G., Bridges, N., Clark, B.C., DeFlores, L., Delapp, D., Dromart, G., Dyar, M.D., Fisk, M., Gondet, B., Grotzinger, J., Herkenhoff, K., Johnson, J., Lacour, J.-L., Langevin, Y., Leshin, L., Lewin, E., Madsen, M.B., Melikechi, N., Mezzacappa, A., Mischna, M.A., Moores, J.E., Newsom, H., Ollila, A., Perez, R., Renno, N., Sirven, J.-B., Tokar, R., de la Torre, M., d'Uston, L., Vaniman, D., Yingst, A., MSL Science Team, M.S, 2013. Soil diversity and hydration as observed by ChemCam at Gale crater, Mars. Science 341, 1238670. https://doi.org/10.1126/science.1238670.

Meslin, P.-Y., Wellington, D., Wiens, R.C., Johnson, J.R., Van Beek, J., Gasnault, O., Sautter, V., Maroger, I., Lasue, J., Beck, P., Bridges, J.C., Cohen, B., Ashley, J.W., Fairén, A.G., Newsom, H., Cousin, A., Forni, O., Calef, F., Rapin, W., Maurice, S., Chide, B., Schröder, S., Goetz, W., Mangold, N., Gabriel, T., Lanza, N., Pinet, P., 2019. Diversity and areal density of iron-nickel meteorites analyzed by Chemcam in Gale Crater. In: 50th Lunar Planet. Sci. Conf. Held 18–22 March, 2019 Woodlands, Texas (LPI Contrib. No. 2132, id.3179 50).

Milliken, R.E., Grotzinger, J.P., Thomson, B.J., 2010. Paleoclimate of Mars as captured by the stratigraphic record in Gale Crater. Geophys. Res. Lett. 37 https://doi.org/10.1029/2009GL041870.

Ming, D.W., Gellert, R., Morris, R.V., Arvidson, R.E., Brückner, J., Clark, B.C., Cohen, B. A., d'Uston, C., Economou, T., Fleischer, I., Klingelhöfer, G., McCoy, T.J., Mittlefehldt, D.W., Schmidt, M.E., Schröder, C., Squyres, S.W., Tréguier, E., Yen, A. S., Zipfel, J., 2008. Geochemical properties of rocks and soils in Gusev Crater, Mars: results of the alpha particle X-ray spectrometer from Cumberland ridge to home plate. J. Geophys. Res. 113, E12S39. https://doi.org/10.1029/2008JE003195.

Morad, S., Aldahan, A.A., 1982. Authigenesis of titanium minerals in two Proterozoic sedimentary rocks from Southern and Central Sweden. SEPM J. Sediment. Res. 52, 1295–1305. https://doi.org/10.1306/212F8120-2B24-11D7-8648000102C1865D.

Morris, R.V., Vaniman, D.T., Blake, D.F., Gellert, R., Chipera, S.J., Rampe, E.B., Ming, D. W., Morrison, S.M., Downs, R.T., Treiman, A.H., Yen, A.S., Grotzinger, J.P., Achilles, C.N., Bristow, T.F., Crisp, J.A., Des Marais, D.J., Farmer, J.D., Fendrich, K. V., Frydenvang, J., Graff, T.G., Morookian, J.-M., Stolper, E.M., Schwenzer, S.P., 2016. Silicic volcanism on Mars evidenced by tridymite in high-SiO_2 sedimentary rock at Gale crater. Proc. Natl. Acad. Sci. 113, 7071–7076. https://doi.org/10.1073/pnas.1607098113.

Morrison, S.M., Downs, R.T., Blake, D.F., Prabhu, A., Eleish, A., Vaniman, D.T., Ming, D. W., Rampe, E.B., Hazen, R.M., Achilles, C.N., Treiman, A.H., Yen, A.S., Morris, R.V., Bristow, T.F., Chipera, S.J., Sarrazin, P.C., Fendrich, K.V., Morookian, J.M., Farmer, J.D., Des Marais, D.J., Craig, P.I., 2018a. Relationships between unit-cell parameters and composition for rock-forming minerals on Earth, Mars, and other extraterrestrial bodies. Am. Mineral. 103, 848–856. https://doi.org/10.2138/am-2018-6123.

Morrison, S.M., Downs, R.T., Blake, D.F., Vaniman, D.T., Ming, D.W., Hazen, R.M., Treiman, A.H., Achilles, C.N., Yen, A.S., Morris, R.V., Rampe, E.B., Bristow, T.F., Chipera, S.J., Sarrazin, P.C., Gellert, R., Fendrich, K.V., Morookian, J.M., Farmer, J. D., Des Marais, D.J., Craig, P.I., 2018b. Crystal chemistry of Martian minerals from Bradbury landing through Naukluft Plateau, Gale crater, Mars. Am. Mineral. 103, 857–871. https://doi.org/10.2138/am-2018-6124.

Mountney, N.P., Russell, A.J., 2004. Sedimentology of cold-climate aeolian sandsheet deposits in the Askja region of northeast Iceland. Sediment. Geol. 166, 223–244. https://doi.org/10.1016/J.SEDGEO.2003.12.007.

Nachon, M., Clegg, S.M., Mangold, N., Schröder, S., Kah, L.C., Dromart, G., Ollila, A., Johnson, J.R., Oehler, D.Z., Bridges, J.C., Le Mouélic, S., Forni, O., Wiens, R.C., Anderson, R.B., Blaney, D.L., Bell, J.F., Clark, B., Cousin, A., Dyar, M.D., Ehlmann, B., Fabre, C., Gasnault, O., Grotzinger, J., Lasue, J., Lewin, E., Léveillé, R., McLennan, S., Maurice, S., Meslin, P.-Y., Rapin, W., Rice, M., Squyres, S.W., Stack, K., Sumner, D.Y., Vaniman, D., Wellington, D., 2014. Calcium sulfate veins characterized by ChemCam/curiosity at Gale crater, Mars. J. Geophys. Res. Planets 119, 1991–2016. https://doi.org/10.1002/2013JE004588.

Newsom, H.E., Edgett, K.S., Fey, D.M., Wiens, R.C., Frydenvang, J., Banham, S.G., Gupta, S., Williams, A.J., Grotzinger, J.P., Mangold, N., Schieber, J., Rivera-Hernandez, F., Belgacem, I., 2018. A buried Aeolian lag deposit at an unconformity between the Murray and Stimson Formations at Marias Pass, Gale Crater, Mars. In: 49th Lunar Planet. Sci. Conf. 19–23 March, 2018, Held Woodlands, Texas LPI Contrib. No. 2083 (id.2263 49).

Nichols, G., 2009. Sedimentology and Stratigraphy. John Wiley & Sons.

O'Connell-Cooper, C.D., Spray, J.G., Thompson, L.M., Gellert, R., Berger, J.A., Boyd, N.I., Desouza, E.D., Perrett, G.M., Schmidt, M., VanBommel, S.J., 2017. APXS-derived chemistry of the Bagnold dune sands: comparisons with Gale Crater soils and the global Martian average. J. Geophys. Res. Planets 122, 2623–2643. https://doi.org/10.1002/2017JE005268.

O'Connell-Cooper, C.D., Thompson, L.M., Spray, J.G., Berger, J.A., VanBommel, S.J., Gellert, R., Boyd, N.I., DeSouza, E., 2018. Chemical diversity of sands within the linear and Barchan Dunes of the Bagnold Dunes, Gale Crater, as revealed by APXS onboard curiosity. Geophys. Res. Lett. 45, 9460–9470. https://doi.org/10.1029/2018GL079026.

Pan, C., Rogers, A.D., 2017. Occurrence and scale of compositional heterogeneity in Martian dune fields: toward understanding the effects of aeolian sorting on Martian sediment compositions. Icarus 282, 56–69. https://doi.org/10.1016/j.icarus.2016.09.021.

Pe-Piper, G., Karim, A., Piper, D.J.W., 2011. Authigenesis of Titania minerals and the mobility of Ti: new evidence from pro-deltaic sandstones, Cretaceous Scotian Basin, Canada. J. Sediment. Res. 81, 762–773. https://doi.org/10.2110/jsr.2011.63.

Potter, S.L., Chan, M.A., Petersen, E.U., Dyar, M.D., Sklute, E., 2011. Characterization of Navajo sandstone concretions: Mars comparison and criteria for distinguishing diagenetic origins. Earth Planet. Sci. Lett. 301, 444–456. https://doi.org/10.1016/J.EPSL.2010.11.027.

Potter-McIntyre, S.L., Chan, M.A., McPherson, B.J., 2014. Concretion formation in Volcaniclastic host rocks: evaluating the role of organics, mineralogy, and geochemistry on early diagenesis. J. Sediment. Res. 84, 875–892. https://doi.org/10.2110/jsr.2014.58.

Rampe, E.B., Ming, D.W., Blake, D.F., Bristow, T.F., Chipera, S.J., Grotzinger, J.P., Morris, R.V., Morrison, S.M., Vaniman, D.T., Yen, A.S., Achilles, C.N., Craig, P.I., Des Marais, D.J., Downs, R.T., Farmer, J.D., Fendrich, K.V., Gellert, R., Hazen, R.M., Kah, L.C., Morookian, J.M., Peretyazhko, T.S., Sarrazin, P., Treiman, A.H., Berger, J. A., Eigenbrode, J., Fairén, A.G., Forni, O., Gupta, S., Hurowitz, J.A., Lanza, N.L., Schmidt, M.E., Siebach, K., Sutter, B., Thompson, L.M., 2017. Mineralogy of an ancient lacustrine mudstone succession from the Murray formation. Gale crater, Mars, Earth and Planetary Science Letters. https://doi.org/10.1016/j.epsl.2017.04.021.

Rampe, E.B., Lapotre, M.G.A., Bristow, T.F., Arvidson, R.E., Morris, R.V., Achilles, C.N., Weitz, C., Blake, D.F., Ming, D.W., Morrison, S.M., Vaniman, D.T., Chipera, S.J., Downs, R.T., Grotzinger, J.P., Hazen, R.M., Peretyazhko, T.S., Sutter, B., Tu, V., Yen, A.S., Horgan, B., Castle, N., Craig, P.I., Des Marais, D.J., Farmer, J., Gellert, R., McAdam, A.C., Morookian, J.M., Sarrazin, P.C., Treiman, A.H., 2018. Sand mineralogy within the Bagnold Dunes, Gale Crater, as observed in situ and from orbit. Geophys. Res. Lett. 45, 9488–9497. https://doi.org/10.1029/2018GL079073.

Rapin, W., Meslin, P.-Y., Maurice, S., Vaniman, D., Nachon, M., Mangold, N., Schröder, S., Gasnault, O., Forni, O., Wiens, R.C., Martínez, G.M., Cousin, A., Sautter, V., Lasue, J., Rampe, E.B., Archer, D., 2016. Hydration state of calcium sulfates in Gale crater, Mars: identification of Bassanite veins. Earth Planet. Sci. Lett. 452, 197–205. https://doi.org/10.1016/J.EPSL.2016.07.045.

Rivera-Hernández, F., Sumner, D.Y., Mangold, N., Stack, K.M., Forni, O., Newsom, H., Williams, A., Nachon, M., L'Haridon, J., Gasnault, O., Wiens, R., Maurice, S., 2019. Using ChemCam LIBS data to constrain grain size in rocks on Mars: proof of concept and application to rocks at Yellowknife Bay and Pahrump Hills, Gale crater. Icarus 321, 82–98. https://doi.org/10.1016/J.ICARUS.2018.10.023.

Rubin, D.M., Hunter, R.E., 1987. Bedform alignment in directionally varying flows. Science 237, 276–278. https://doi.org/10.1126/science.237.4812.276.

Schieber, J., Bish, D., Coleman, M., Reed, M., Hausrath, E.M., Cosgrove, J., Gupta, S., Minitti, M.E., Edgett, K.S., Malin, M., 2017. Encounters with an unearthly mudstone: understanding the first mudstone found on Mars. Sedimentology 64, 311–358. https://doi.org/10.1111/sed.12318.

Schuenemeyer, J., Drew, L., 2011. Statistics for Earth and Environmental Scientists.

Schwenzer, S.P., Bridges, J.C., Wiens, R.C., Conrad, P.G., Kelley, S.P., Leveille, R., Mangold, N., Martín-Torres, J., McAdam, A., Newsom, H., Zorzano, M.P., Rapin, W., Spray, J., Treiman, A.H., Westall, F., Fairén, A.G., Meslin, P.-Y., 2016. Fluids during diagenesis and sulfate vein formation in sediments at Gale crater, Mars. Meteorit. Planet. Sci. 51, 2175–2202. https://doi.org/10.1111/maps.12668.

Sharp, R.P., 1963. Wind ripples. J. Geol. 71, 617–636. https://doi.org/10.1086/626936.

Siebach, K.L., Baker, M.B., Grotzinger, J.P., McLennan, S.M., Gellert, R., Thompson, L.M., Hurowitz, J.A., 2017a. Sorting out compositional trends in sedimentary rocks of the Bradbury group (Aeolis Palus), Gale crater, Mars. J. Geophys. Res. Planets 122, 295–328. https://doi.org/10.1002/2016JE005195.

Siebach, K.L., McLennan, S.M., Fedo, C.M., 2017b. Geochemistry of the Stimson Sandstone, Gale Crater, Mars. In: 48th Lunar Planet. Sci. Conf. Held 20–24 March 2017, Woodlands, Texas. LPI Contrib. No. 1964 (id.2499 48).

Stack, K.M., Grotzinger, J.P., Lamb, M.P., Gupta, S., Rubin, D.M., Kah, L.C., Edgar, L.A., Fey, D.M., Hurowitz, J.A., McBride, M., Rivera-Hernández, F., Sumner, D.Y., Van Beek, J.K., Williams, R.M.E., Aileen Yingst, R., 2019. Evidence for plunging river plume deposits in the Pahrump Hills member of the Murray formation, Gale crater, Mars. Sedimentology 66, 1768–1802. https://doi.org/10.1111/sed.12558.

Stockstill-Cahill, K.R., Anderson, F.S., Hamilton, V.E., 2008. A study of low-albedo deposits within Amazonis Planitia craters: evidence for locally derived ultramafic to mafic materials. J. Geophys. Res. 113, E07008 https://doi.org/10.1029/2007JE003036.

Swanson, T., Mohrig, D., Kocurek, G., 2016. Aeolian dune sediment flux variability over an annual cycle of wind. Sedimentology 63, 1753–1764. https://doi.org/10.1111/sed.12287.

Swanson, T., Mohrig, D., Kocurek, G., Cardenas, B.T., Wolinsky, M.A., 2019. Preservation of autogenic processes and allogenic forcings in set-scale Aeolian architecture I: numerical experiments. J. Sediment. Res. 89, 728–740. https://doi.org/10.2110/jsr.2019.42.

Thomson, B.J., Bridges, N.T., Milliken, R., Baldridge, A., Hook, S.J., Crowley, J.K., Marion, G.M., de Souza Filho, C.R., Brown, A.J., Weitz, C.M., 2011. Constraints on the origin and evolution of the layered mound in Gale Crater, Mars using Mars Reconnaissance Orbiter data. Icarus 214, 413–432. https://doi.org/10.1016/J.ICARUS.2011.05.002.

Treiman, A.H., Bish, D.L., Vaniman, D.T., Chipera, S.J., Blake, D.F., Ming, D.W., Morris, R.V., Bristow, T.F., Morrison, S.M., Baker, M.B., Rampe, E.B., Downs, R.T., Filiberto, J., Glazner, A.F., Gellert, R., Thompson, L.M., Schmidt, M.E., Le Deit, L., Wiens, R.C., McAdam, A.C., Achilles, C.N., Edgett, K.S., Farmer, J.D., Fendrich, K.V., Grotzinger, J.P., Gupta, S., Morookian, J.M., Newcombe, M.E., Rice, M.S., Spray, J. G., Stolper, E.M., Sumner, D.Y., Vasavada, A.R., Yen, A.S., 2016. Mineralogy, provenance, and diagenesis of a potassic basaltic sandstone on Mars: CheMin X-ray diffraction of the Windjana sample (Kimberley area, Gale Crater). J. Geophys. Res. Planets 121, 75–106. https://doi.org/10.1002/2015JE004932.

Vaniman, D.T., Bish, D.L., Ming, D.W., Bristow, T.F., Morris, R.V., Blake, D.F., Chipera, S. J., Morrison, S.M., Treiman, A.H., Rampe, E.B., Rice, M., Achilles, C.N., Grotzinger, J.P., McLennan, S.M., Williams, J., Bell, J.F., Newsom, H.E., Downs, R.T., Maurice, S., Sarrazin, P., Yen, A.S., Morookian, J.M., Farmer, J.D., Stack, K., Milliken, R.E., Ehlmann, B.L., Sumner, D.Y., Berger, G., Crisp, J.A., Hurowitz, J.A., Anderson, R., Des Marais, D.J., Stolper, E.M., Edgett, K.S., Gupta, S., Spanovich, N., Agard, C., Alves Verdasca, J.A., Anderson, R., Archer, D., Armiens-Aparicio, C., Arvidson, R., Atlaskin, E., Atreya, S., Aubrey, A., Baker, B., Baker, M., Balic-Zunic, T., Baratoux, D., Baroukh, J., Barraclough, B., Bean, K., Beegle, L., Behar, A., Bender, S., Benna, M., Bentz, J., Berger, J., Berman, D., Blanco Avalos, J.J., Blaney, D., Blank, J., Blau, H., Bleacher, L., Boehm, E., Botta, O., Bottcher, S., Boucher, T., Bower, H., Boyd, N., Boynton, B., Breves, E., Bridges, J., Bridges, N., Brinckerhoff, W., Brinza, D., Brunet, C., Brunner, A., Brunner, W., Buch, A., Bullock, M., Burmeister, S., Cabane, M., Calef, F., Cameron, J., Campbell, J.I., Cantor, B., Caplinger, M., Caride Rodriguez, J., Carmosino, M., Carrasco Blazquez, I., Charpentier, A., Choi, D., Clark, B., Clegg, S., Cleghorn, T., Cloutis, E., Cody, G., Coll, P., Conrad, P., Coscia, D., Cousin, A., Cremers, D., Cros, A., Cucinotta, F., d'Uston, C., Davis, S., Day, M.K., de la Torre Juarez, M., DeFlores, L., DeLapp, D., DeMarines, J., Dietrich, W., Dingler, R., Donny, C., Drake, D., Dromart, G., Dupont, A., Duston, B., Dworkin, J., Dyar, M.D., Edgar, L., Edwards, C., Edwards, L., Ehresmann, B., Eigenbrode, J., Elliott, B., Elliott, H., Ewing, R., Fabre, C., Fairen, A., Farley, K., Fassett, C., Favot, L., Fay, D., Fedosov, F., Feldman, J., Feldman, S., Fisk, M., Fitzgibbon, M., Flesch, G., Floyd, M., Fluckiger, L., Forni, O., Fraeman, A., Francis, R., Francois, P., Franz, H., Freissinet, C., French, K.L., Frydenvang, J., Gaboriaud, A., Gailhanou, M., Garvin, J., Gasnault, O., Geffroy, C., Gellert, R., Genzer, M., Glavin, D., Godber, A., Goesmann, F., Goetz, W., Golovin, D., Gomez Gomez, F., Gomez-Elvira, J., Gondet, B., Gordon, S., Gorevan, S., Grant, J., Griffes, J., Grinspoon, D., Guillemot, P., Guo, J., Guzewich, S., Haberle, R., Halleaux, D., Hallet, B., Hamilton, V., Hardgrove, C., Harker, D., Harpold, D., Harri, A.-M., Harshman, K., Hassler, D., Haukka, H., Hayes, A., Herkenhoff, K., Herrera, P., Hettrich, S., Heydari, E., Hipkin, V., Hoehler, T., Hollingsworth, J., Hudgins, J., Huntress, W., Hviid, S., Iagnemma, K., Indyk, S., Israel, G., Jackson, R., Jacob, S., Jakosky, B., Jensen, E., Jensen, J.K., Johnson, J., Johnson, M., Johnstone, S., Jones, A., Jones, J., Joseph, J., Jun, I., Kah, L., Kahanpaa, H., Kahre, M., Karpushkina, N., Kasprzak, W., Kauhanen, J., Keely, L., Kemppinen, O., Keymeulen, D., Kim, M.-H., Kinch, K., King, P., Kirkland, L., Kocurek, G., Koefoed, A., Kohler, J., Kortmann, O., Kozyrev, A., Krezoski, J., Krysak, D., Kuzmin, R., Lacour, J.L., Lafaille, V., Langevin, Y., Lanza, N., Lasue, J., Le Mouelic, S., Lee, E.M., Lee, Q.-M., Lees, D., Lefavor, M., Lemmon, M., Malvitte, A.L., Leshin, L., Leveille, R., Lewin-Carpintier, E., Lewis, K., Li, S., Lipkaman, L., Little, C., Litvak, M., Lorigny, E., Lugmair, G., Lundberg, A., Lyness, E., Madsen, M., Mahaffy, P., Maki, J., Malakhov, A., Malespin, C., Malin, M., Mangold, N., Manhes, G., Manning, H., Marchand, G., Marin Jimenez, M., Martin Garcia, C., Martin, D., Martin, M., Martinez-Frias, J., Martin-Soler, J., Martin-Torres, F.J., Mauchien, P., McAdam, A., McCartney, E., McConnochie, T., McCullough, E., McEwan, I., McKay, C., McNair, S., Melikechi, N., Meslin, P.-Y., Meyer, M., Mezzacappa, A., Miller, H., Miller, K., Minitti, M., Mischna, M., Mitrofanov, I., Moersch, J., Mokrousov, M., Molina Jurado, A., Moores, J., Mora-Sotomayor, L., Mueller-Mellin, R., Muller, J.-P., Munoz Caro, G., Nachon, M., Navarro Lopez, S., Navarro-Gonzalez, R., Nealson, K., Nefian, A., Nelson, T., Newcombe, M., Newman, C., Nikiforov, S., Niles, P., Nixon, B., Noe Dobrea, E., Nolan, T., Oehler, D., Ollila, A., Olson, T., Owen, T., de Pablo Hernandez, M.A., Paillet, A., Pallier, E., Palucis, M., Parker, T., Parot, Y., Patel, K., Paton, M., Paulsen, G., Pavlov, A., Pavri, B., Peinado-Gonzalez, V., Pepin, R., Peret, L., Perez, R., Perrett, G., Peterson, J., Pilorget, C., Pinet, P., Pla-Garcia, J., Plante, I., Poitrasson, F., Polkko, J., Popa, R., Posiolova, L., Posner, A., Pradler, I., Prats, B., Prokhorov, V., Purdy, S.W., Raaen, E., Radziemski, L., Rafkin, S., Ramos, M., Raulin, F., Ravine, M., Reitz, G., Renno, N., Richardson, M., Robert, F., Robertson, K., Rodriguez Manfredi, J.A., Romeral-Planello, J.J., Rowland, S., Rubin, D., Saccoccio, M., Salamon, A., Sandoval, J., Sanin, A., Sans Fuentes, S.A., Saper, L., Sautter, V., Savijarvi, H., Schieber, J., Schmidt, M., Schmidt, W., Scholes, D.D., Schoppers, M., Schroder, S., Schwenzer, S., Sebastian Martinez, E., Sengstacken, A., Shterts, R., Siebach, K., Siili, T., Simmonds, J., Sirven, J.-B., Slavney, S., Sletten, R., Smith, M., Sobron Sanchez, P., Spray, J., Squyres, S., Stalport, F., Steele, A., Stein, T., Stern, J., Stewart, N., Stipp, S.L.S., Stoiber, K., Sucharski, B., Sullivan, R., Summons, R., Sun, V., Supulver, K., Sutter, B., Szopa, C., Tan, F., Tate, C., Teinturier, S., ten Kate, I., Thomas, P., Thompson, L., Tokar, R., Toplis, M., Torres Redondo, J., Trainer, M., Tretyakov, V., Urqui-O'Callaghan, R., Van Beek, J., Van Beek, T., VanBommel, S., Varenikov, A., Vasavada, A., Vasconcelos, P., Vicenzi, E., Vostrukhin, A., Voytek, M., Wadhwa, M., Ward, J., Webster, C., Weigle, E., Wellington, D., Westall, F., Wiens, R.C., Wilhelm, M.B., Williams, A., Williams, R., Williams, R.B.M., Wilson, M., Wimmer-Schweingruber, R., Wolff, M., Wong, M., Wray, J., Wu, M., Yana, C., Yingst, A., Zeitlin, C., Zimdar, R., Zorzano Mier, M.-P., 2014. Mineralogy of a mudstone at Yellowknife Bay, Gale Crater, Mars. Science (80-.) 343, 1243480. https://doi.org/10.1126/science.1243480.

Vasavada, A.R., Grotzinger, J.P., Arvidson, R.E., Calef, F.J., Crisp, J.A., Gupta, S., Hurowitz, J., Mangold, N., Maurice, S., Schmidt, M.E., Wiens, R.C., Williams, R.M.E., Yingst, R.A., 2014. Overview of the Mars Science Laboratory mission: Bradbury Landing to Yellowknife Bay and beyond. J. Geophys. Res. Planets 119, 1134–1161. https://doi.org/10.1002/2014JE004622.

Watkins, J.A., Grotzinger, J., Stein, N., Banham, S.G., Gupta, S., Rubin, D., Stack, K.M., Edgett, K.S., 2016. Paleotopography of erosional unconformity, base of Stimson Formation, Gale Crater, Mars. In: 47th Lunar Planet. Sci. Conf. Held March 21–25, 2016 Woodlands, Texas. LPI Contrib. No. 1903, 47, p. 2939 (2939).

Wiens, R.C., Maurice, S., Barraclough, B., Saccoccio, M., Barkley, W.C., Bell, J.F., Bender, S., Bernardin, J., Blaney, D., Blank, J., Bouyé, M., Bridges, N., Bultman, N., Caïs, P., Clanton, R.C., Clark, B., Clegg, S., Cousin, A., Cremers, D., Cros, A., DeFlores, L., Delapp, D., Dingler, R., D'Uston, C., Darby Dyar, M., Elliott, T., Enemark, D., Fabre, C., Flores, M., Forni, O., Gasnault, O., Hale, T., Hays, C., Herkenhoff, K., Kan, E., Kirkland, L., Kouach, D., Landis, D., Langevin, Y., Lanza, N., LaRocca, F., Lasue, J., Latino, J., Limonadi, D., Lindensmith, C., Little, C., Mangold, N., Manhes, G., Mauchien, P., McKay, C., Miller, E., Mooney, J., Morris, R. V., Morrison, L., Nelson, T., Newsom, H., Ollila, A., Ott, M., Pares, L., Perez, R., Poitrasson, F., Provost, C., Reiter, J.W., Roberts, T., Romero, F., Sautter, V., Salazar, S., Simmonds, J.J., Stiglich, R., Storms, S., Striebig, N., Thocaven, J.-J., Trujillo, T., Ulibarri, M., Vaniman, D., Warner, N., Waterbury, R., Whitaker, R., Witt, J., Wong-Swanson, B., 2012. The ChemCam instrument suite on the Mars Science Laboratory (MSL) rover: body unit and combined system tests. Space Sci. Rev. 170, 167–227. https://doi.org/10.1007/s11214-012-9902-4.

Wiens, R.C., Maurice, S., Lasue, J., Forni, O., Anderson, R.B., Clegg, S., Bender, S., Blaney, D., Barraclough, B.L., Cousin, A., Deflores, L., Delapp, D., Dyar, M.D., Fabre, C., Gasnault, O., Lanza, N., Mazoyer, J., Melikechi, N., Meslin, P.-Y., Newsom, H., Ollila, A., Perez, R., Tokar, R.L., Vaniman, D., 2013. Pre-flight calibration and initial data processing for the ChemCam laser-induced breakdown

spectroscopy instrument on the Mars Science Laboratory rover. Spectrochim. Acta Part B At. Spectrosc. 82, 1–27. https://doi.org/10.1016/j.sab.2013.02.003.

Williams, R.M.E., Grotzinger, J.P., Dietrich, W.E., Gupta, S., Sumner, D.Y., Wiens, R.C., Mangold, N., Malin, M.C., Edgett, K.S., Maurice, S., Forni, O., Gasnault, O., Ollila, A., Newsom, H.E., Dromart, G., Palucis, M.C., Yingst, R.A., Anderson, R.B., Herkenhoff, K.E., Le Mouélic, S., Goetz, W., Madsen, M.B., Koefoed, A., Jensen, J.K., Bridges, J.C., Schwenzer, S.P., Lewis, K.W., Stack, K.M., Rubin, D., Kah, L.C., Bell, J. F., Farmer, J.D., Sullivan, R., Van Beek, T., Blaney, D.L., Pariser, O., Deen, R.G., MSL Science Team, M.S, 2013. Martian fluvial conglomerates at Gale crater. Science 340, 1068–1072. https://doi.org/10.1126/science.1237317.

Wray, J.J., 2013. Gale crater: the Mars Science Laboratory/Curiosity Rover landing site. Int. J. Astrobiol. 12, 25–38. https://doi.org/10.1017/S1473550412000328.

Yen, A.S., Ming, D.W., Vaniman, D.T., Gellert, R., Blake, D.F., Morris, R.V., Morrison, S. M., Bristow, T.F., Chipera, S.J., Edgett, K.S., Treiman, A.H., Clark, B.C., Downs, R.T., Farmer, J.D., Grotzinger, J.P., Rampe, E.B., Schmidt, M.E., Sutter, B., Thompson, L. M., 2017. Multiple stages of aqueous alteration along fractures in mudstone and sandstone strata in Gale Crater, Mars. Earth Planet. Sci. Lett. 471, 186–198. https://doi.org/10.1016/J.EPSL.2017.04.033.